J. Fluid Mech. (2019), *vol.* 880, *pp.* 388–429. © Cambridge University Press 2019
doi:10.1017/jfm.2019.727

Supersonic turbulent boundary layer drag control using spanwise wall oscillation

Jie Yao[1] **and Fazle Hussain**[1,†]

[1]Department of Mechanical Engineering, Texas Tech University, Lubbock, TX 79409, USA

(Received 20 February 2019; revised 29 August 2019; accepted 30 August 2019;
first published online 9 October 2019)

Spanwise wall oscillation has been extensively studied to explore possible drag control methods, mechanisms and efficacy – particularly for incompressible flows. We performed direct numerical simulation for fully developed turbulent channel flow to establish how effective spanwise wall oscillation is when the flow is compressible and also to document its drag reduction ($\mathcal{DR}$) trend with Mach number. Drag reduction $\mathcal{DR}$ is first investigated for three different bulk Mach numbers $M_b = 0.3$, 0.8 and 1.5 at a fixed bulk Reynolds number $Re_b = 3000$. At a given velocity amplitude A^+ ($= 12$), $\mathcal{DR}$ at $M_b = 0.3$ agrees with the strictly incompressible case; at $M_b = 0.8$, $\mathcal{DR}$ exhibits a similar trend to that at $M_b = 0.3$: $\mathcal{DR}$ increases with the oscillation period T^+ to a maximum and then decreases gradually. However, at $M_b = 1.5$, $\mathcal{DR}$ monotonically increases with T^+. In addition, the maximum $\mathcal{DR}$ is found to increase with M_b. For $M_b = 1.5$, similar to the incompressible case, $\mathcal{DR}$ increases with A^+, but the rate of increase decreases at larger A^+. Unlike the flow behaviour when incompressible, the flow surprisingly relaminarizes when it is supersonic (at $A^+ = 18$ and $T^+ = 300$) – this enigmatic behaviour requires further detailed studies for different domain sizes, Re_b and M_b. The Reynolds number effect on $\mathcal{DR}$ is also investigated. Although $\mathcal{DR}$ generally decreases with Re_b, it is less affected at small T^+, but drops rapidly at large T^+. We introduce a simple scaling for the oscillation period as $T^* = T_C^+ l_I^+ / l_C^+$, with l_I^+ and l_C^+ denoting the mean streak spacing for incompressible and compressible cases, respectively. At the same semi-local Reynolds number $Re_{\tau c}^* \equiv Re_\tau \sqrt{\overline{\rho}_c/\overline{\rho}_w}/(\overline{\mu}_c/\overline{\mu}_w)$ (subscripts c and w denote quantities at the channel centre and wall, respectively), $\mathcal{DR}$ as a function of T^* exhibits good agreement between the supersonic and strictly incompressible cases, with the optimal oscillation period becoming M_b-invariant as $T_{opt}^* \approx 100$.

Key words: compressible boundary layers, drag reduction, turbulence control

1. Introduction

The pursuit of skin-friction drag control in turbulent boundary layers is of great importance not only for fundamental research but also for practical engineering applications (Spalart & McLean 2011). For example, considering the large numbers of aircraft in transportation, where more than 50 % of the drag is from skin friction, even

† Email address for correspondence: fazle.hussain@ttu.edu

https://doi.org/10.1017/jfm.2019.727 Published online by Cambridge University Press

a minor reduction in skin friction could result in sizeable fuel saving, which could also lead to environmental pollution reduction. Driven by this objective, numerous drag control techniques, either passive (Bechert *et al.* 1997; Min & Kim 2004; Rothstein 2010; Nakanishi, Mamori & Fukagata 2012) or active (Jung, Mangiavacchi & Akhavan 1992; Choi, Moin & Kim 1994; Schoppa & Hussain 1998; Berger *et al.* 2000; Yao *et al.* 2017), have been proposed and investigated. Among them, open-loop active control techniques have certain advantages. First, compared with passive methods, they can generally lead to a higher drag reduction ($\mathcal{DR}$) in a wide range of flow conditions. Second, in contrast to the closed-loop methods, they can be applied independently of the instantaneous flow field, obviating the need for complex sensors and actuation.

Spanwise wall oscillation (SWO), which only involves two control parameters (i.e. the maximum spanwise wall velocity A and the time period of the oscillation T), is one of the simplest and extensively studied open-loop active methods. It was first explored by Jung *et al.* (1992), who demonstrated that $\mathcal{DR}$ of as high as 40 % in turbulent channel flow can be achieved at a friction Reynolds number $Re_\tau = 200$ with T^+ of the order of 10^2 (the superscript $+$ indicates that the quantity is scaled by viscous wall units). Later, Baron & Quadrio (1995) estimated the control power input and demonstrated that net power saving is possible if the control parameters are appropriately chosen. Inspired by these pioneering works, numerous studies have been performed for various types of flows, such as channel flow (Choi, Xu & Sung 2002; Quadrio & Ricco 2004; Ricco & Quadrio 2008; Touber & Leschziner 2012; Agostini, Touber & Leschziner 2014), pipe flow (Orlandi & Fatica 1997; Quadrio & Sibilla 2000) and boundary layer flow (Laadhari, Skandaji & Morel 1994; Lardeau & Leschziner 2013; Hack & Zaki 2014; Skote, Mishra & Wu 2015, 2019).

Here, we summarize some of the key results regarding drag control using SWO mainly in turbulent channel flows. Choi *et al.* (2002) performed direct numerical simulation (DNS) for Re_τ up to 400 with $A^+ = 5$, 10 and 20, and T^+ between 50 and 200, and observed a significant decrease in $\mathcal{DR}$ as Re_τ increased from 100 to 400. They proposed a parameter V_c^+, which combines the length and acceleration scales of the spanwise Stokes layer, to link the control parameters to $\mathcal{DR}$. Quadrio & Ricco (2003) analysed the transient behaviour of flow within the first few cycles after applying SWO. They found that the spanwise velocity from DNS matches the analytical solution of the second Stokes problem. Later, Quadrio & Ricco (2004) systematically examined the effects of the control parameters on $\mathcal{DR}$ at $Re_\tau = 200$. For a given T^+, $\mathcal{DR}$ increases with A^+, but the rate of increase saturates as A^+ becomes large. In addition, only SWO with lower amplitudes demonstrated net energy savings. Xu & Huang (2005) studied the transient response of the Reynolds stress transport under SWO. Later, Ricco & Quadrio (2008) showed that $\mathcal{DR}$ drops by around 5 % as Re_τ increases from 200 to 400. They also derived a Stokes-layer-based parameter, which relates to $\mathcal{DR}$ linearly. Touber & Leschziner (2012) performed DNS at $Re_\tau = 200$ and 500 with suboptimal oscillation periods in order to highlight the importance of phase-wise turbulence statistics. Yakeno, Hasegawa & Kasagi (2014) investigated the modification of quasi-streamwise vortices by SWO and its relationship to $\mathcal{DR}$ using conditional averaging techniques.

Due to the continual increase of computational capability, studies have been slowly progressing towards higher Reynolds numbers, since the influence of Re_τ on $\mathcal{DR}$ is an essential issue. The drag reduction is often assumed to decrease with Reynolds number following a power law, i.e. $\mathcal{DR} \approx Re_\tau^{-\gamma}$, with the scaling exponent γ determined empirically. Agostini *et al.* (2014) performed DNS studies

https://doi.org/10.1017/jfm.2019.727 Published online by Cambridge University Press

up to $Re_\tau = 1000$ with $T^+ = 100$ and 200 and suggested $\gamma = 0.2$. In addition, they found that the lower $\mathcal{DR}$ at higher Re_τ might be attributed to the presence of large-scale structures (Hutchins & Marusic 2007; Marusic, Mathis & Hutchins 2010). Moarref & Jovanović (2012) developed a model-based approach where they used eddy-viscosity-enhanced linearization of the flow with control in conjunction with turbulence modelling to determine skin-friction drag. They found that the scaling exponent γ is around 0.15 up to $Re_\tau = 1000$. Unfortunately, their method relies on the availability of statistical results of the uncontrolled flow at the same Re_τ and currently does not lend itself to being very useful at very high Re_τ. The studies by Gatti & Quadrio (2013), based on DNS with rather small computational domains up to $Re_\tau = 1000$ and a few points at $Re_\tau = 2100$, confirmed that maximum $\mathcal{DR}$ indeed decreases rapidly with $\gamma = 0.2$. These results were also confirmed by Hurst, Yang & Chung (2014) with DNS using full-size computational domains. In addition, they also found that the scaling parameter γ has a strong dependence on control parameters, typically ranging between 0.1 and 0.5. Gatti & Quadrio (2016) performed detailed Reynolds number dependence studies for a wide range of control parameters using a very small domain size. Following the idea for surface roughness (Jiménez 2004) and riblets (García-Mayoral & Jiménez 2011), they proposed a more physical approach to characterize $\mathcal{DR}$ via a vertical shift of the mean velocity profile. Based on this prediction, $\mathcal{DR}$ presents a mild logarithmic decrease with Re_τ, and they claimed that a sizeable amount of $\mathcal{DR}$ could be achieved at Re_τ values of practical applications. Recently, Yao, Chen & Hussain (2019) extended the DNS study up to $Re_\tau = 2000$ and found that the decreased $\mathcal{DR}$ at higher Re_τ can be attributed to the weakened effect of suppressing near-wall large-scale turbulence.

All the studies mentioned above were made for incompressible flows. However, in practical applications, such as aircraft, the Mach number is often higher than the value where the incompressible assumption holds (i.e. typically less than 0.3). During the past few decades, compressible turbulent channel flow (CTCF) has also been extensively studied, mainly through DNS. The CTCF between isothermal walls was first studied by Coleman, Kim & Moser (1995) at bulk Mach numbers $M_b = 1.5$ and 3 and bulk Reynolds numbers $Re_b = 3000$ and 4880. They found that the mean density and temperature gradients result in enhanced coherence of near-wall streaks when compared to incompressible cases. In addition, the compressibility effects caused by the mean property variations were dominant, compared with those caused by thermodynamic fluctuations. Later, Huang, Coleman & Bradshaw (1995) analysed the DNS results of Coleman *et al.* (1995) and found that the difference between Reynolds and Favre averages was small, mainly differing at the region close to the wall. They proposed a semi-local scaling based on wall shear stress and local properties to better collapse the turbulent statistics in the near-wall region with the incompressible data. Morinishi, Tamano & Nakabayashi (2004) performed DNS of CTCF between adiabatic and isothermal walls. It was found that Morkovin's hypothesis, which generally claimed that the compressible shear flow dynamics follows the incompressible case, was not applicable to the near-wall asymptotic behaviour of the wall-normal turbulence intensity. In addition, they observed that the near-wall streaks are independent of thermal wall boundary conditions if semi-local units are used. Foysi, Sarkar & Friedrich (2004) further analysed the semi-local scaling for Reynolds stresses in CTCF with isothermal walls. They found that the streamwise Reynolds stress increased, while the wall-normal and spanwise Reynolds stresses decreased when compared with the incompressible case. They concluded that the semi-local scaling gives better matches for Reynolds stresses as compared to the classical wall scaling.

https://doi.org/10.1017/jfm.2019.727 Published online by Cambridge University Press

Trettel & Larsson (2016) investigated the failure of the van Driest transformation for the isothermal wall case, and they derived a novel mean velocity transformation which can better incorporate the wall-normal density and viscosity gradient effect. Later, Modesti & Pirozzoli (2016) performed detailed DNS study of Reynolds and Mach number effects for the isothermal CTCF at $M_b = 1.5$ and 3 and Re_b up to 17 000. They compared different compressibility transformations and concluded that the transformation introduced by Trettel & Larsson (2016) performs best for collapsing mean velocity profiles. For the Reynolds stresses, they found that the semi-local transformation by Huang *et al.* (1995) performs well, with the only exception for the streamwise Reynolds stress peak, which is typically higher than that of the incompressible case. Patel *et al.* (2015) and Patel, Boersma & Pecnik (2016) studied the effect of variable density and viscosity on the scaling of turbulence statistics and near-wall turbulence for the low-Mach-number cases. Unlike the constant-property turbulent flow, where mean velocity and turbulent statistics can be expressed as a function of wall-normal distance and friction Reynolds number Re_τ, they showed that, for the variable-property flows, turbulence statistics strongly depend on the semi-local Reynolds number $Re_\tau^* \equiv Re_\tau \sqrt{\overline{\rho}/\overline{\rho}_w}/(\overline{\mu}/\overline{\mu}_w)$ (where overbar and subscript w denote Reynolds averaging and wall quantity, respectively). They also found that the enhancement of the streamwise Reynolds stress peak can be associated with the strengthening of large-scale low-speed streaks in the buffer layer.

Compared with numerous works that have been done for drag control in incompressible flow, far fewer studies have been performed for compressible flows. Duan & Choudhari (2012, 2014) conducted DNS of spatially developing turbulent boundary layers over riblets with a broad range of spacings and found a 7 % drag reduction. Gomez, Flutet & Sagaut (2009), by extending the FIK identity (Fukagata, Iwamoto & Kasagi 2002) to compressible flow, demonstrated that the dominant contributor to the skin friction is still the Reynolds shear stress and that the small difference from the incompressible flow comes from the variable dynamic viscosity. Fang, Lu & Shao (2010) carried out a large-eddy simulation of CTCF under SWO at $M_b = 0.5$, with emphasis on heat transport and its relationship with momentum transport. Subsequently, Ni *et al.* (2016) conducted DNS of the supersonic turbulent boundary layer at a free-stream Mach number of 2.9 under SWO where they found that, although the velocity and temperature statistics are disturbed differently, the Reynolds analogy is still preserved if the effect of the Stokes layer can be removed properly. Zhe *et al.* (2016) investigated the effects of uniform blowing or suction on the skin friction in hypersonic spatially developing turbulent boundary layers at a free-stream Mach number of 6. Consistent with the incompressible case (Kametani & Fukagata 2011; Kametani *et al.* 2015), they demonstrated that uniform blowing reduces the skin friction while uniform suction increases it; the turbulent fluctuations exhibit the opposite trend. Kametani *et al.* (2017) studied the effects of uniform blowing or suction on CTCF and found that $\mathcal{DR}$ and the net energy savings are hardly affected by the Mach number. In addition, the effect of control on thermodynamic quantities, like temperature, density and turbulent Mach number, is small.

In the present work, we investigate the compressibility effect on drag control using SWO in turbulent channel flow. The rest of paper is organized as follows. In § 2, the governing equations, the numerical scheme and simulation parameters are presented. Section 3 presents drag control results for different M_b values at $Re_b = 3000$, including the effect of control parameters on $\mathcal{DR}$, flow statistics and coherent structures. In § 4, the effect of Reynolds number on $\mathcal{DR}$ is also investigated. Comparisons between the supersonic and incompressible flows at comparable semi-local Reynolds numbers are performed, and a scaling transformation is proposed for the oscillation period to better match $\mathcal{DR}$. Finally, conclusions are drawn in § 5.

https://doi.org/10.1017/jfm.2019.727 Published online by Cambridge University Press

2. Methodologies

2.1. *Governing equations*

The Navier–Stokes equations can be used to entirely describe the compressible turbulent flow and be expressed in the conservative form

$$\frac{\partial \rho}{\partial t} + \frac{\partial \rho u_i}{\partial x_i} = 0, \tag{2.1}$$

$$\frac{\partial \rho u_i}{\partial t} + \frac{\partial \rho u_i u_j}{\partial x_j} = -\frac{\partial p}{\partial x_i} + \frac{\partial \sigma_{ij}}{\partial x_j} + f_i, \tag{2.2}$$

$$\frac{\partial e}{\partial t} + \frac{\partial (e+p)u_j}{\partial x_j} = \frac{\partial \sigma_{ij} u_i - q_j}{\partial x_j} + f_i u_i, \tag{2.3}$$

where ρ is the density, u_i the velocity component, p the pressure, q_j the components of the heat flux vector, σ_{ij} the viscous stress tensor and $e = \rho(e_s + u_i u_i/2)$ the total energy per unit mass, which is the sum of internal energy e_s and kinetic energy. The Einstein summation convention is used.

The system of the equation remains unclosed until the thermal and caloric equation of state is defined. In the present study, the fluid considered is a perfect gas, $p = \rho R T_e$, with R the universal gas constant per unit gas. Thus, the internal energy is a function of the temperature only: $e_s = c_v T_e$, with c_v the specific heat at constant volume, $c_v = R/(\gamma - 1)$, in which $\gamma = c_p/c_v$ is the specific heat ratio, where c_p is the specific heat at constant pressure.

The fluid is Newtonian with the viscous shear stress given as

$$\sigma_{ij} = 2\mu \left(\mathcal{S}_{ij} - \tfrac{1}{3} \mathcal{S}_{kk} \delta_{ij} \right), \tag{2.4}$$

where $\mathcal{S}_{ij}$ is the rate of strain tensor,

$$\mathcal{S}_{ij} = \frac{1}{2} \left(\frac{\partial u_i}{\partial x_j} + \frac{\partial u_j}{\partial x_i} \right), \tag{2.5}$$

and μ is the dynamical viscosity, assumed to be a function of temperature only. For gases, the viscosity is an increasing function of temperature, whose dependence on temperature is given by Sutherland's law:

$$\mu = \mu_0 \frac{T_{e0} + S}{T_e + S} \left(\frac{T_e}{T_{e0}} \right)^{3/2}, \tag{2.6}$$

where μ_0 and T_{e0} are reference values and S is a constant. Throughout, $S = 110.4$ K and $T_{e0} = 293.15$ K (Morinishi *et al.* 2004).

Finally, the heat flux q_j is modelled through the Fourier law:

$$q_j = -k \frac{\partial T_e}{\partial x_j}, \tag{2.7}$$

where $k = c_p \mu / Pr$ is the thermal conductivity, with $Pr = 0.72$.

https://doi.org/10.1017/jfm.2019.727 Published online by Cambridge University Press

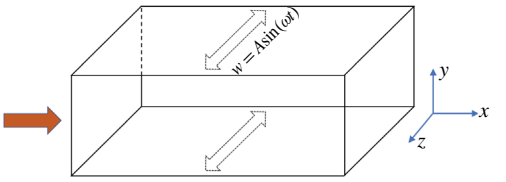


FIGURE 1. (Colour online) Schematic of the turbulent channel flow under SWO with amplitude A and angular frequency ω; x, y and z denote the streamwise, wall-normal and spanwise directions, respectively.

2.2. *Flow configuration*

Figure 1 shows a schematic of the turbulent channel flow, where x and z represent homogeneous streamwise and spanwise directions, respectively, in which periodic boundary conditions are imposed, and y denotes the wall-normal direction. The isothermal wall boundary condition is employed, and the no-slip boundary conditions for velocities are applied, i.e. $(u_i)_w = 0$. For the controlled cases, both walls move in unison with a periodic spanwise velocity, namely

$$w_w(t) = A\sin(\omega t), \tag{2.8}$$

where A the velocity amplitude and $\omega = 2\pi/T$ is the angular frequency.

Following Coleman *et al.* (1995), the bulk Reynolds number is defined as $Re_b = \rho_b U_b h/\mu_w$, where μ_w is the dynamics viscosity on the wall, and bulk density ρ_b and bulk mean velocity U_b are defined as

$$\rho_b = \frac{1}{2h}\int_{-h}^{h}\langle\rho\rangle\,\mathrm{d}y, \tag{2.9}$$

$$U_b = \frac{1}{2h\rho_b}\int_{-h}^{h}\langle\rho u\rangle\,\mathrm{d}y, \tag{2.10}$$

and the bulk Mach number is defined as

$$M_b = U_b/c_w, \tag{2.11}$$

where c_w is the speed of sound at the wall temperature. Following standard practice (Coleman *et al.* 1995), a spatially constant body force f_1 is applied in the streamwise direction in order to enforce constant mass flow rate in time, and the corresponding power spent is added to the right-hand side of the total energy equation.

2.3. *Numerical set-up*

A DNS of CTCF is performed with an in-house code. The governing equations are discretized based on the finite-difference method with a seventh-order upwind-biased scheme (Rai & Moin 1991; Mittal & Moin 1997) for the convective terms and eighth-order centred scheme for the viscous terms. Time integration is done by using the low-storage third-order Runge–Kutta scheme. The mesh spacing is constant in the wall-parallel direction, and a mapping function is used in the wall-normal direction to cluster mesh points towards the wall. The DNS is carried out in a rectangular box whose sizes in the x, y, z directions are denoted as L_x, L_y, L_z. For the uncontrolled

https://doi.org/10.1017/jfm.2019.727 Published online by Cambridge University Press

Case	Re_b	Re_τ	$Re^*_{\tau c}$	M_b	$N_x \times N_y \times N_z$	Δx^+	Δy^+	Δz^+
C3kM03	3000	190	187	0.3	$384 \times 129 \times 192$	9.3	0.45–6.2	6.2
C3kM08	3000	198	174	0.8	$384 \times 129 \times 192$	9.7	0.47–6.4	6.5
C3kM15	3000	219	145	1.5	$512 \times 129 \times 256$	8.1	0.52–7.1	5.4
C8kM08	7667	466	381	0.8	$768 \times 193 \times 384$	11.4	0.73–9.9	7.6
C8kM15	7667	506	336	1.5	$1024 \times 257 \times 512$	9.3	0.58–8.2	6.2

TABLE 1. Details of the numerical discretization employed for the present simulations. The computational box size is $6\pi h \times 2h \times 2\pi h$ (h is the half-channel height) for all cases, and N_x, N_y and N_z are the numbers of grid sizes in x, y and z directions. Here $Re^*_{\tau c}$ indicates the semi-local Reynolds number Re^*_τ at the half-channel height.

cases, all simulations are initiated with parabolic velocity profile plus superimposed random fluctuations and with uniform values for the temperature and density. For the controlled cases, all simulations start with the same initial condition of an uncontrolled fully developed turbulent channel flow at the same Re_b and M_b.

First, DNS is conducted at three different Mach numbers $M_b = 0.3$ (nearly incompressible case), 0.8 (subsonic case) and 1.5 (supersonic case) with a fixed $Re_b = 3000$. The wall velocity amplitude was fixed at $A^+ \ (\equiv A/u_\tau) = 12$ to enable comparison with previous incompressible results (Quadrio, Ricco & Viotti 2009; Touber & Leschziner 2012; Hurst *et al.* 2014). The oscillation period is varied as $T^+ (\equiv Tu_\tau^2/\nu_w) \in [25, 50, 75, 100, 150, 200, 250, 300]$. (Throughout the paper, the control parameters are all non-dimensionalized by the wall units of the uncontrolled cases.) Then, two additional forcing amplitudes $A^+ = 6$ and 18 are applied at $M_b = 1.5$ to quantify the amplitude effect. Finally, to further investigate the Reynolds number effect, additional simulations are also performed at a higher $Re_b = 7667$ for $M_b = 0.8$ and 1.5 cases. Details of the simulation parameters (i.e. grid sizes and resolutions) are given in table 1. All simulations are carried out with a constant time-marching step $\Delta t^+ = 0.025$, with time averaging for statistics taken over at least $t^+ (\equiv tu_\tau^2/\nu) = 10\,000$ after the initial transition. The grid resolution employed here is nearly the same as that used by Modesti & Pirozzoli (2016), who demonstrated the sufficiency of this resolution by a detailed sensitivity study. The computational box size is $6\pi h \times 2h \times 2\pi h$ (h is half of the channel height) for all cases. Note that, for incompressible flow, the adequacy of this box size has been well established for both the uncontrolled (Lozano-Duran & Jiménez 2014) and controlled (Gatti & Quadrio 2013; Hurst *et al.* 2014) cases. As the typical size of structures enlarges as M_b increases, it might still be necessary to justify the adequacy of the current domain size for compressible cases. In the Appendix, we provide a detailed study and justification of the domain size on skin friction and drag reduction for the $Re_b = 3000$ and $M_b = 1.5$ case.

For comparison, drag control for incompressible flows at two different friction Reynolds numbers Re_τ is carried out. The numerical details are provided in table 2. The code used for the incompressible case is the same as the one used in our previous studies (Yao *et al.* 2019), built around the main solver developed by Lee & Moser (2015). The incompressible Navier–Stokes equations are solved using the method of Kim, Moin & Moser (1987), in which equations for the wall-normal vorticity and the Laplacian of the wall-normal velocity are time-advanced. This formulation has the advantage of satisfying the continuity constraint exactly while eliminating the pressure. A Fourier–Galerkin method is used in the streamwise and spanwise directions, while

https://doi.org/10.1017/jfm.2019.727 Published online by Cambridge University Press

Case	Re_b	Re_τ	$N_x \times N_y \times N_z$	Δx^+	Δy^+	Δz^+
I2kM00	2136	141	$384 \times 128 \times 192$	6.9	0.08–3.3	4.6
I6kM00	5882	340	$768 \times 192 \times 384$	8.3	0.12–5.3	5.6

TABLE 2. Details of the numerical discretization employed for the incompressible turbulent channel simulations. The computational box size is $6\pi h \times 2h \times 2\pi h$ for all cases, and N_x, N_y and N_z are the numbers of grid sizes.

a seventh-order B-spline collocation method is used in the wall-normal direction. A low-storage implicit–explicit scheme based on third-order Runge–Kutta for the nonlinear terms and Crank–Nicolson for the viscous terms is used for time advance. The flow is driven by a pressure gradient, which is adjusted in time to ensure that the mass flux through the channel always remains constant. For more details about the code, the numerical methods and how the simulations are run, see Lee & Moser (2015).

2.4. *Code validation*

In the following, both Reynolds (ensemble) and Favre averaging (Huang *et al.* 1995)

$$\phi = \overline{\phi} + \phi' = \widetilde{\phi} + \phi'' \tag{2.12}$$

are employed for flow statistics. In (2.12), $\overline{\phi}$ denotes Reynolds averaging (in the homogeneous space direction and in time) with fluctuation ϕ' satisfying

$$\overline{\phi'} = 0, \tag{2.13}$$

and $\widetilde{\phi}$ denotes Favre averaging with fluctuation ϕ'' defined as

$$\widetilde{\phi} = \overline{\rho\phi}/\overline{\rho}, \tag{2.14}$$

$$\phi'' = \phi - \widetilde{\phi}. \tag{2.15}$$

Considering the periodic nature of the actuation, phase averaging is also employed and defined as

$$\langle\phi\rangle(y, \varphi) = \frac{1}{N}\sum_{n=0}^{N-1}\frac{1}{L_x}\frac{1}{L_z}\int_0^{L_x}\int_0^{L_z}\phi(x, y, z, \varphi + 2\pi n)\,\mathrm{d}x\,\mathrm{d}z, \tag{2.16}$$

where the averaging is applied at a fixed phase φ in the homogeneous directions, $\langle\cdot\rangle$ indicates a phase-averaged quantity and N is the number of cycles during the integration time.

The Reynolds stress tensor is denoted as $\tau_{ij} = \overline{\rho}R_{ij}$, with $R_{ij} = \widetilde{u_i''u_j''} = \widetilde{u_iu_j} - \widetilde{u}_i\widetilde{u}_j$. Hereinafter, quantities made non-dimensional with respect to the wall friction velocity $u_\tau = \sqrt{\tau_w/\rho_w}$ and the viscous length scale ($\delta_\nu = \nu_w/u_\tau$, where $\nu = \mu/\rho$ is the kinematic viscosity) are denoted with superscript $+$. The friction Reynolds number is defined as the ratio of outer to viscous length scales, hence $Re_\tau = h/\delta_\nu = u_\tau h/\nu_w$. Huang *et al.* (1995) suggested that normalizing the mean velocity and Reynolds stress profiles with respect to suitable semi-local wall units based on the local density and viscosity (i.e. $u_\tau^* = \sqrt{\tau_w/\overline{\rho}}$, $\delta_\nu^* = \overline{\nu}/u_\tau^*$) yields better collapse of the flow statistics

https://doi.org/10.1017/jfm.2019.727 Published online by Cambridge University Press

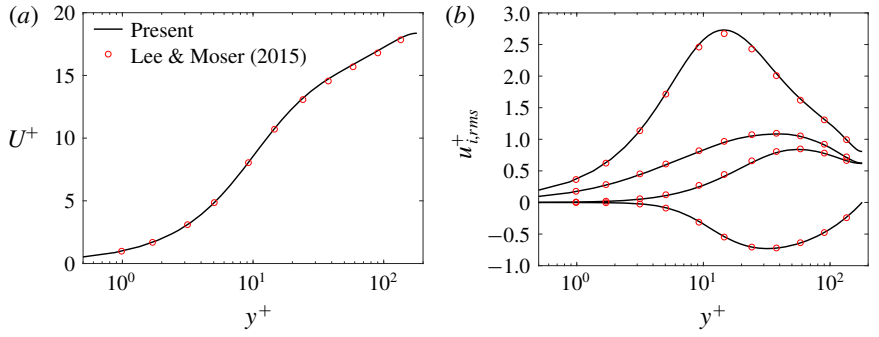


FIGURE 2. (Colour online) (*a*) Mean velocity ($U^+(y^+)$) and (*b*) root-mean-square of velocity fluctuations for the uncontrolled case at $Re_b = 2880$ and $M_b = 0.3$. Solid lines represent our DNS results and circles are results from Lee & Moser (2015) at $Re_\tau = 180$.

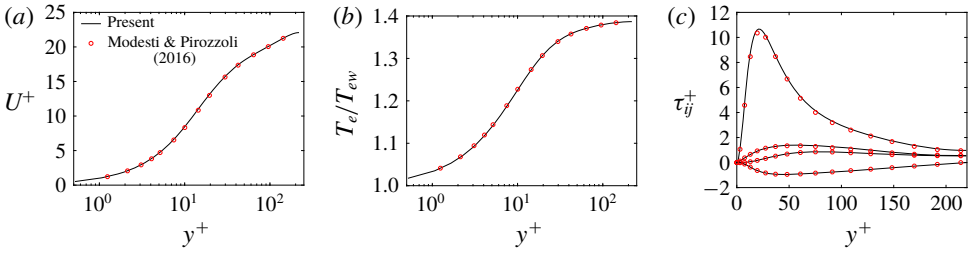


FIGURE 3. (Colour online) Comparison with DNS data of Modesti & Pirozzoli (2016) (circles) for $Re_b = 3000$ and $M_b = 1.5$: (*a*) mean velocity ($U^+(y^+)$), (*b*) mean temperature (T_e/T_{ew}) and (*c*) Reynolds normal and shear stresses (τ_{ij}).

with incompressible flows. Accordingly, the semi-local Reynolds number is defined as $Re^*_\tau = h/\delta^*_v = Re_\tau \sqrt{(\overline{\rho}/\overline{\rho}_w)}/(\overline{\mu}/\overline{\mu}_w)$. Note that for isothermal CTCF, $Re^*_\tau = Re_\tau$ at the wall and decreases towards the channel centre.

The compressible solver is first tested in the nearly incompressible case and compared with the strictly incompressible data of Lee & Moser (2015). Figure 2 shows the mean velocity profile U^+ and root-mean-square of velocity fluctuations, as well as the Reynolds shear stress ($\overline{u'v'}$) for the uncontrolled case at $Re_b = 2880$ and $M_b = 0.3$. Excellent agreement is observed in the mean-velocity profiles, the velocity fluctuations and Reynolds shear stress; except for the slight difference at the peak of the streamwise velocity fluctuations, which is known to be quite sensitive to discretization methods and mesh resolution (Bernardini, Pirozzoli & Orlandi 2014). In addition to the incompressible case, the code is further validated with a supersonic case at $Re_b = 3000$ and $M_b = 1.5$. Figure 3 shows a comparison of mean velocity U^+, temperature Te and Reynolds stresses τ_{ij} between our results and those of Modesti & Pirozzoli (2016). Our results show good congruence in all the flow statistics, suggesting the accuracy of our solver and adequacy of the grid resolution.

3. Spanwise wall oscillation at $Re_b = 3000$

3.1. *Drag reduction at* $A^+ = 12$

Figure 4 shows the early time evolution ($t^+ < 7000$) of the skin friction coefficient $C_f(t) = 2\tau_w(t)/(\rho_b U_b^2)$ normalized by the uncontrolled value $C_{f,0}$ for different

https://doi.org/10.1017/jfm.2019.727 Published online by Cambridge University Press

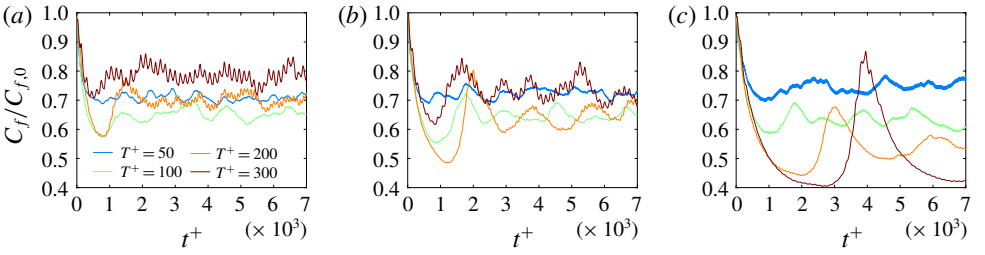


FIGURE 4. (Colour online) Initial time evolution ($t^+ \leqslant 7000$) of skin friction normalized by the uncontrolled case $C_f/C_{f,0}$ at different wall oscillation period T^+ with $A^+ = 12$ for $Re_b = 3000$ and (*a*) $M_b = 0.3$, (*b*) $M_b = 0.8$ and (*c*) $M_b = 1.5$.

oscillation periods T^+ with $A^+ = 12$ at different M_b values. Note that at a given time t, $C_f(t)$ is obtained by averaging in the homogeneous directions. Some interesting features of figure 4 are summarized below.

(i) First, for the nearly incompressible cases (i.e. $M_b = 0.3$), $C_f(t)$ initially rapidly decreases as the oscillation starts, and the decrease rates are very similar for all T^+. Then, C_f reaches a temporal minimum before approaching the statistical quasi-steady low-drag state. The long-time-scale undulation of C_f, which has also been observed by others (Quadrio & Ricco 2003; Touber & Leschziner 2012), is mainly because of the existence of large-scale turbulent structures – their augmentation/abatement leads to increase/decrease of C_f. (Note that similar undulations also occur for flows in the absence of SWO.) First, the computational domain size, although considerably large when compared with the length scale of near-wall structures, accommodates only a few of these large-scale structures in both x and z directions. Therefore, averaging over the wall does not result in a converged constant value. Another issue is the periodic boundary condition imposed during the simulation. It has been shown that very large-scale structures, which can be significantly longer than typical streak length of 10^3 wall units, can exist (Guala, Hommema & Adrian 2006; Lozano-Durán & Jiménez 2014). Since the streamwise domain of our simulation is around 4×10^3 wall units, these structures are not fully decorrelated because of x-periodicity of the domain, and hence recycled.

(ii) For the compressible cases, the long-time-scale undulation of C_f becomes more apparent, especially for high drag reduction cases. One reason is that, as M_b increases, the length scale of the large-scale structures increases; hence the computational domain includes even fewer of these structures (e.g. see figure 14). In addition, due to the relatively small Reynolds number involved ($Re^*_{\tau c} < 200$), the drag-reducing flow is barely turbulent and becomes transitional. One example is the case of $T^+ = 300$ at $M_b = 1.5$ (figure 4*c*), where C_f experiences continued rapid increases and decreases. Flow is almost relaminarized at $t^+ \approx 2600$; the flow then regenerates the vortical structures to reach another peak at $t^+ = 4100$; and this quasi-cyclical process continues for many periods (see figure 16 for a longer time evolution). These in combination explain the larger temporal fluctuation of spatially averaged skin friction $C_f(t)$ observed for $M_b = 0.8$ and 1.5 cases.

(iii) For the nearly incompressible cases (i.e. $M_b = 0.3$), C_f hardly responds to the actuation at small T^+ (i.e. $T^+ = 50$); while substantial small-scale C_f undulations, with half the wall oscillation period, occur for large T^+, which is due to the turbulence responding to the wall actuation – the near-wall structures have enough time to

https://doi.org/10.1017/jfm.2019.727 Published online by Cambridge University Press

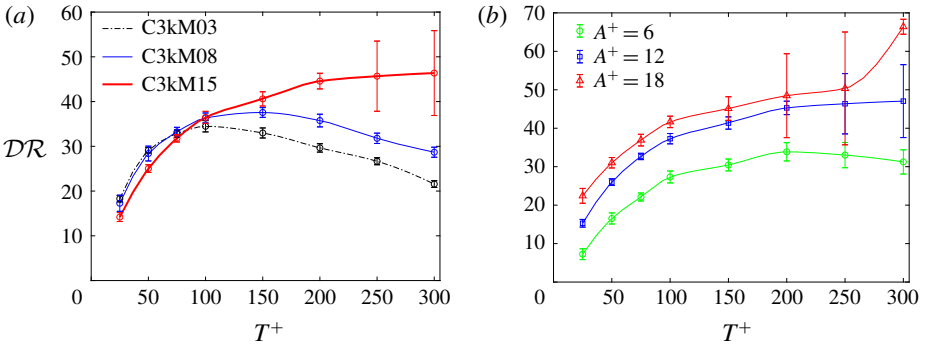


FIGURE 5. (Colour online) Drag reduction rate $\mathcal{DR}$ (%) as a function of T^+ at $Re_b = 3000$ for (*a*) different M_b at $A^+ = 12$ and (*b*) different A^+ at $M_b = 1.5$. The error bars indicate the corresponding uncertainty of $\mathcal{DR}$.

develop their inner dynamics between successive activation of the near-wall Stokes layer (Quadrio & Ricco 2004; Touber & Leschziner 2012). However, as M_b increases, undulation in C_f at small T^+ increases (note that the thicker curve for $T^+ = 50$ in figure 4(*c*) is due to very high-frequency oscillations, not visible in this compressed time curve). This high-frequency behaviour is further compounded by the fact that dispassion at this high frequency is significantly enhanced as the thermodynamic properties are altered (discussed in detail later).

We define the extent of drag reduction as

$$\mathcal{DR}\,(\%) = 1 - \overline{C}_f/\overline{C}_{f,0}. \tag{3.1}$$

And its uncertainty is calculated by following the procedure in Gatti & Quadrio (2016). First, the standard uncertainty $\sigma_{\overline{C}_f}$ of $\overline{C}_f$ is calculated via an autoregressive method as described by Oliver *et al.* (2014). Then the standard uncertainty $\sigma_{\mathcal{DR}}$ of $\mathcal{DR}$ is obtained by propagating the standard uncertainty of $\overline{C}_f$ for the uncontrolled and controlled cases (assuming they are independent variables (Gatti & Quadrio 2013)), i.e. $\sigma_{\mathcal{DR}} = (\overline{C}_f/\overline{C}_{f,0})\sqrt{(\sigma_{\overline{C}_f}/\overline{C}_f)^2 + (\sigma_{\overline{C}_{f,0}}/\overline{C}_{f,0})^2}$. Finally, the uncertainty is extended to a 95 % confidence interval $\delta_{\mathcal{DR}} = z\sigma_{\mathcal{DR}}$, where $z = 1.96$ is the standardized 95 % confidence interval of a normalized Gaussian probability density function. The uncertainty of $\mathcal{DR}$ is reported in the text when applicable and plotted as error bars in the figures. Note that since the control parameters considered are mainly located in the region of negative net power saving, the energy cost and total net power saving rate are not addressed here.

Figure 5(*a*) shows $\mathcal{DR}$ against the oscillation period T^+ with an amplitude of $A^+ = 12$ for all M_b cases at $Re_b = 3000$. First, for the nearly incompressible $M_b = 0.3$ case, the present results agree with those of Touber & Leschziner (2012), Gatti & Quadrio (2013), Hurst *et al.* (2014) and Yao *et al.* (2019) at $Re_\tau = 200$. The maximum drag reduction $\mathcal{DR}_{max} = 34.8\,\% \pm 0.9\,\%$ with the optimal oscillation period $T^+_{opt} = 100$; both of these agree well with the results of Yao *et al.* (2019). Note that our results are also close to the 36.4 % of Hurst *et al.* (2014) and 37.4 % of Gatti & Quadrio (2016) (the latter is slightly higher due to smaller domain size used, which causes overestimation of $\mathcal{DR}$ in the region close to the optimal period, as reported by Gatti & Quadrio (2013)). For $M_b = 0.8$, $\mathcal{DR}$ exhibits a similar trend to the $M_b = 0.3$ case, namely $\mathcal{DR}$

https://doi.org/10.1017/jfm.2019.727 Published online by Cambridge University Press

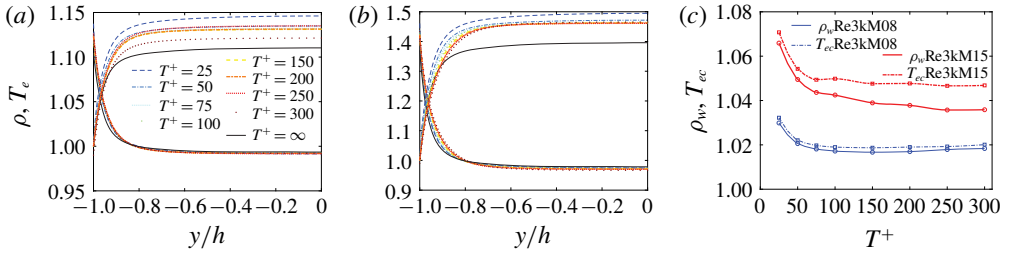


FIGURE 6. (Colour online) Mean density $\overline{\rho}$ and temperature $\overline{T}_e$ profiles for different oscillating period T^+ with $A^+ = 12$ for (*a*) $M_b = 0.8$ and (*b*) $M_b = 1.5$ with $Re_b = 3000$. (*c*) The temperature at the channel centre $\overline{T}_{ec}$ and density at the wall $\overline{\rho}_w$ as a function of T^+ for both cases.

increases with T^+ to a maximum and then decreases gradually. However, compared with the $M_b = 0.3$ case, $\mathcal{DR}$ at $M_b = 0.8$ slightly decreases at small T^+ (i.e. $\leqslant 100$), but increases at large T^+. The optimal oscillation period is shifted to $T^+_{opt} = 150$, with $\mathcal{DR}_{max} = 37.6\,\% \pm 1.1\,\%$ – slightly higher than that obtained at $M_b = 0.3$. At $M_b = 1.5$, $\mathcal{DR}$ further decreases at small T^+ but, interestingly, increases monotonically with T^+. At $T^+ = 300$, the largest oscillation period considered, $\mathcal{DR}$ reaches $47.1\,\% \pm 8.1\,\%$. The large uncertainty is attributed to the low Reynolds number effect, where the flow continues to undulate in time between laminar and turbulent states.

3.2. *Mean density and temperature profiles*

Profiles of the Reynolds-averaged density $\overline{\rho}$ and temperature $\overline{T}_e$ for different oscillation periods T^+ are displayed in figures 6(*a*) and 6(*b*) for $M_b = 0.8$ and 1.5, respectively. The results for the $M_b = 0.3$ case are not shown since the temperature and density are barely changed. For both $M_b = 0.8$ and 1.5 cases, $\overline{T}_e$ rises steeply near the wall and reaches a plateau in the core region; correspondingly, $\overline{\rho}$ decreases rapidly near the wall and then reaches a plateau in the channel core (Foysi *et al.* 2004). The temperature at the centre of the channel $\overline{T}_{ec}$ and density at the wall $\overline{\rho}_w$ increase with M_b, which is due to enhanced viscous heating. Under SWO, as a consequence of the dissipation of the Stokes layer, a significant increase of the mean temperature first occurs near the wall and then diffuses over the whole channel, particularly for cases with smaller T^+ (or larger ω^+), as expected. It is different with the turbulent boundary layer case (Ni *et al.* 2016), where the effect of the Stokes layer on the mean temperature profiles is mainly limited to the near-wall region, as the time needed for diffusion along the wall direction, before the flow is advected downstream, is not available. Accordingly, under SWO, the mean density $\overline{\rho}$ at the wall also increases, while $\overline{\rho}$ is only slightly affected in the core region, where the compressible effect is rather weak. The temperature at the centre $\overline{T}_{ec}$ and the density on the wall $\overline{\rho}_w$ as a function of T^+ are further displayed in figure 6(*c*). Both $\overline{T}_{ec}$ and $\overline{\rho}_w$ increase as T^+ decreases (or ω^+ increases), with a rapid increase of $\overline{T}_{ec}$ and ρ_w for very small T^+. The variation of these thermodynamic properties will be found to play a role in affecting the drag control performance; this role is different from the control with uniform blowing and suction (Kametani *et al.* 2017), where $\overline{\rho}_w$ and $\overline{T}_{ec}$ are not significantly altered.

https://doi.org/10.1017/jfm.2019.727 Published online by Cambridge University Press

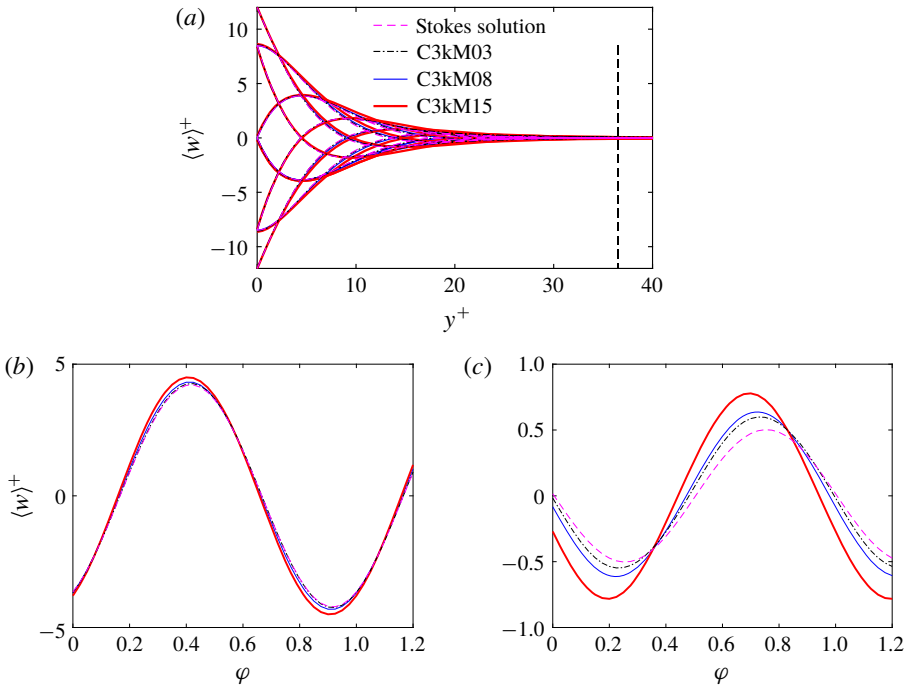


FIGURE 7. (Colour online) Phase-averaged spanwise velocity profiles $\langle w\rangle^+$ for $T^+ = 100$ and $A^+ = 12$ as a function of (a) wall-normal coordinate y^+ and as function of oscillation phase φ at (b) $\eta = 1$ ($y^+ \approx 6$) and (c) $\eta = \pi$ ($y^+ \approx 19$). Note that the incompressible laminar Stokes layer solutions are also included for comparison, with the vertical dashed line in (a) denoting the Stokes layer thickness.

3.3. *Mean spanwise velocity profiles*

In the case of wall-oscillation-induced fluid only, the flow develops the Stokes layer, whose profiles, in the incompressible limit, are given by (Batchelor 1967)

$$W(y, t) = A\mathrm{e}^{-\eta}\sin(\omega t - \eta), \tag{3.2}$$

where $\eta = y\sqrt{\omega/2\nu}$.

Previous incompressible studies have shown that the Stokes layer induced in turbulent channel flow agrees with the laminar analytical solution for relatively small oscillation period T^+, where the Stokes layer is within the viscous sublayer (Quadrio & Sibilla 2000; Touber & Leschziner 2012). For the compressible case, the Stokes layer also depends on the fluid properties, like density and viscosity, whose values change along the wall-normal direction and change with the phase of oscillation, as well as the control parameters, i.e. wall oscillation amplitude A^+ and frequency ω^+. Hence, equation (3.2), in general, is no longer valid. However, it might still be interesting to compare the phase-averaged spanwise velocity with the incompressible laminar Stokes layer profiles. Figure 7(a) shows the phase-averaged spanwise velocity $\langle w\rangle^+$ profiles for $T^+ = 100$ for all M_b cases, along with the incompressible laminar Stokes flow solution (3.2). The laminar Stokes layer thickness is $\delta^+ = \sqrt{4\pi T^+}$ in wall units, which is $\delta^+ = 35.4$ for $T^+ = 100$. A detailed comparison of the spanwise

https://doi.org/10.1017/jfm.2019.727 Published online by Cambridge University Press

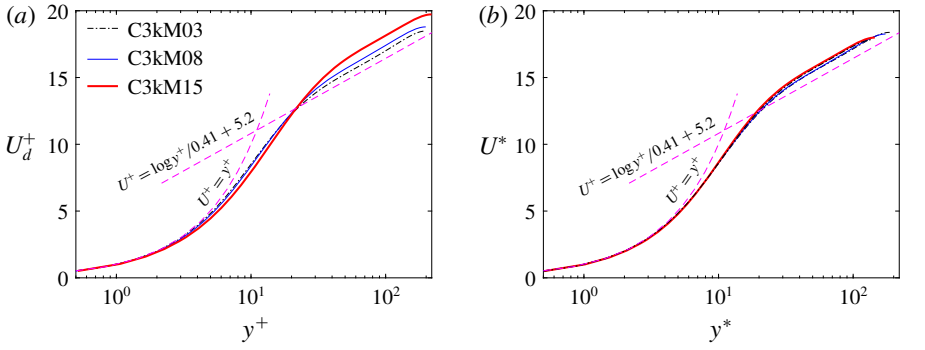


FIGURE 8. (Colour online) Mean velocity profiles transformed according to (*a*) van Driest (1951) and (*b*) Trettel & Larsson (2016) for $Re_b = 3000$ at all M_b values. The dashed lines represent the law of the wall: linear law $U^+ = y^+$ and log law $U^+ = (1/\kappa)\ln y^+ + B$ with $\kappa = 0.41$ and $B = 5.2$.

velocity profiles as a function of the oscillation phase φ at different wall-normal locations y^+ is presented in figure 7(*b*,*c*). Interestingly, very close to the wall, e.g. at $\eta = 1$ (corresponding to $y^+ = 6$), $\langle w\rangle^+$ is quite similar to the Stokes layer profiles even for the $M_b = 1.5$ case. However, further away from the wall, $\langle w\rangle^+$ deviates from the incompressible laminar Stokes profile, even for the $M_b = 0.3$ case. In particular, the phase difference between DNS and incompressible laminar Stokes profile increases with M_b, and the amplitude of $\langle w\rangle^+$ decays slower for larger M_b cases. Note that with increasing M_b, the fluid viscosity near the wall increases; hence the phase variation along the wall-normal direction decreases below that in the incompressible case – progressively more at even higher M_b.

3.4. *Mean streamwise velocity profiles*

It is known that classical wall unit scaling fails in collapsing the velocity profiles when the compressibility effect is present. To incorporate the effect of density variation, the van Driest transformation (van Driest 1951), defined as

$$U_d^+ = \int_0^{U^+} \sqrt{\frac{\overline{\rho}}{\overline{\rho}_w}}\,\mathrm{d}U^+, \tag{3.3}$$

has typically been employed to collapse velocity profiles of supersonic flows with those of incompressible flows. The success of the density-weighted scaling can be attributed to Morkovin's hypothesis, which assumes that, for moderate Mach numbers, the compressibility effect on turbulence could be accounted for by the mean density variations alone. The van Driest transformation has been shown to be good in collapsing velocity profiles of supersonic flows over adiabatic walls (Duan, Beekman & Martin 2010; Pirozzoli & Bernardini 2011; Hadjadj *et al.* 2015). However, the van Driest transformation fails to capture the correct intercept of the log law for diabatic walls, and the deviation increases for cases with strong heat flux (Duan *et al.* 2010). Figure 8(*a*) shows the mean velocity profiles based on the van Driest transformation as a function of y^+ for the uncontrolled cases for all three M_b cases. Also included in the figure are the law of the wall: $U^+ = y^+$ and $U^+ = (1/\kappa)\ln y^+ + B$, where

https://doi.org/10.1017/jfm.2019.727 Published online by Cambridge University Press

$\kappa = 0.41$ and $B = 5.2$. The van Driest transformation yields the correct log-layer profile. Consistent with the previous results (Modesti & Pirozzoli 2016; Patel *et al.* 2016), the van Driest transformation visibly undershoots the incompressible velocity profile in the viscous sublayer and overshoots in the log layer, especially for the $M_b = 1.5$ case.

Trettel & Larsson (2016) derived a transformation that could incorporate the wall-normal density and viscosity gradients:

$$U^* = \int_0^{U^+} \sqrt{\frac{\overline{\rho}}{\overline{\rho}_w}} \left[1 + \frac{1}{2\overline{\rho}}\frac{\mathrm{d}\overline{\rho}}{\mathrm{d}y}y - \frac{1}{\overline{\mu}}\frac{\mathrm{d}\overline{\mu}}{\mathrm{d}y}y\right] \mathrm{d}U^+, \tag{3.4}$$

which has been shown to successfully collapse mean velocity profiles for supersonic channel flows with isothermally cooled walls (Modesti & Pirozzoli 2016; Zhang, Duan & Choudhari 2018). By rescaling the Navier–Stokes equations using the local mean properties and semi-local friction velocity, Patel *et al.* (2016) derived an equivalent mean velocity transform as

$$U^* = \int_0^{U_d} \left(1 + \frac{y}{Re_\tau^*}\frac{\mathrm{d}Re_\tau^*}{\mathrm{d}y}\right) \mathrm{d}U_d. \tag{3.5}$$

Figure 8(*b*) further shows the mean velocity profiles according to the transformation of Trettel & Larsson (2016) for all three M_b cases. Note that the wall-normal distance is non-dimensionalized using the semi-local scaling y^* $(= yRe_\tau^*)$. Apparently, the limitation of the van Driest transformation is overcome by this transformation, which yields overall good collapse among all the profiles across the whole wall-normal range.

The mean velocity profiles based on both van Driest and Trettel–Larsson transformations under SWO with different T^+ at $A^+ = 12$ for all M_b cases are displayed in figure 9. Consistent with the incompressible control cases (Touber & Leschziner 2012; Hurst *et al.* 2014), under control the velocity profiles in the log-law region show a characteristic upward shift when the u_τ value for each controlled flow is used for scaling; the magnitude of the upward shift is roughly proportional to $\mathcal{DR}$. This is rather interesting but not surprising, because with increasing $\mathcal{DR}$ the viscous layer becomes thicker, and the log layer is, therefore, shifted upward (not unlike similar shift by roughness on the wall). At this low Re_b, the mean velocity profiles slowly transform towards laminar profiles for high $\mathcal{DR}$ cases; hence the log law becomes less distinct, which is more evident at large T^+ for the $M_b = 1.5$ case (figure 9*f*).

3.5. *Reynolds stress and FIK identity*

The effect of control on turbulent fluctuations is further scrutinized. Figure 10 shows the Reynolds normal stresses (τ_{11}, τ_{22} and τ_{33}) as a function of y_0^+ with different oscillation period T^+ at $A^+ = 12$. To highlight the absolute changes under control, the Reynolds stresses are normalized with the wall shear stress $\tau_{w,0}$ for the uncontrolled cases. Note that scaling with the controlled wall shear stress would be indicative of universal viscous scaling, which we do not focus on here.

Let us first focus on the streamwise Reynolds stress τ_{11}. For the uncontrolled case, the peak value increases as M_b increases; and the peak location also slightly moves outward, namely changing from $y^+ \approx 15$ at $M_b = 0.3$ to $y^+ \approx 20$ at $M_b = 1.5$. Note that when semi-local coordinates y^* are used, a better match among different

https://doi.org/10.1017/jfm.2019.727 Published online by Cambridge University Press

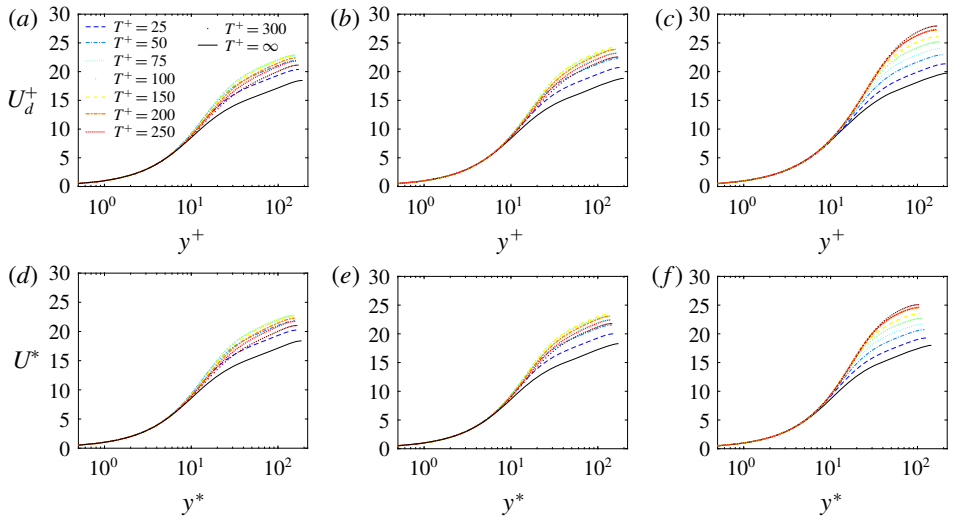


FIGURE 9. (Colour online) Transformed mean streamwise velocity profiles for different oscillation periods T^+ with $A^+ = 12$ for (*a*,*d*) $M_b = 0.3$, (*b*,*e*) $M_b = 0.8$ and (*c*,*f*) $M_b = 1.5$. (*a–c*) The van Driest transformation and (*d–f*) the Trettel–Larsson transformation. Note that $T^+ = \infty$ (the lowest curve) denotes the uncontrolled case.

M_b cases, especially for the peak location, can be obtained – to be discussed later. Under control, the stress is overall suppressed in the whole range of wall-normal coordinate, especially for the large $\mathcal{DR}$ cases. Compared to the uncontrolled case, the peak location moves away from the wall under control, which is consistent with the observation in the strictly incompressible cases (Hurst *et al.* 2014; Yao *et al.* 2019) as well as for other control methods (Choi *et al.* 1994; Deng *et al.* 2014). The peak value and the peak location also seem to change systematically with $\mathcal{DR}$: namely, strong suppression of the peak value and large outward shift of peak location occur for large $\mathcal{DR}$.

In contrast to the increase of the peak of τ_{11}, the peak of wall-normal Reynolds stress τ_{22} for the uncontrolled case decreases with increasing M_b. Similar is the case for both spanwise Reynolds stress τ_{33} and Reynolds shear stress τ_{12}. We give a qualitative explanation of the difference of increasing M_b on τ_{11} and τ_{22}. The reason is that, as M_b increases, temperature increases, and so does the viscosity – suppressing the ejection and sweep events of near-wall streamwise vortices, thus leading to lower values of the peak in τ_{22} (Sciacovelli, Cinnella & Gloerfelt 2017). This is different from τ_{11}, where the peak is increased due to mean shear ($\mathrm{d}U/\mathrm{d}y$), which is higher in the case of high M_b. The effect of control on wall-normal stress is similar to that on streamwise Reynolds stress.

However, the behaviour of spanwise Reynolds stress τ_{33} under control is different: it develops a near-wall peak at large T^+ for $M_b = 0.3$, which even exceeds the uncontrolled cases indicating the reduced effectiveness of control at large T^+. A similar effect was explained by Touber & Leschziner (2012) via both statistical and structural approaches. Statistically, a production term associated with the shear strain of the Stokes layer significantly contributes to the budget of τ_{33} and enhances it. The production term is typically much lower at smaller T^+, due to the fact that the level of

https://doi.org/10.1017/jfm.2019.727 Published online by Cambridge University Press

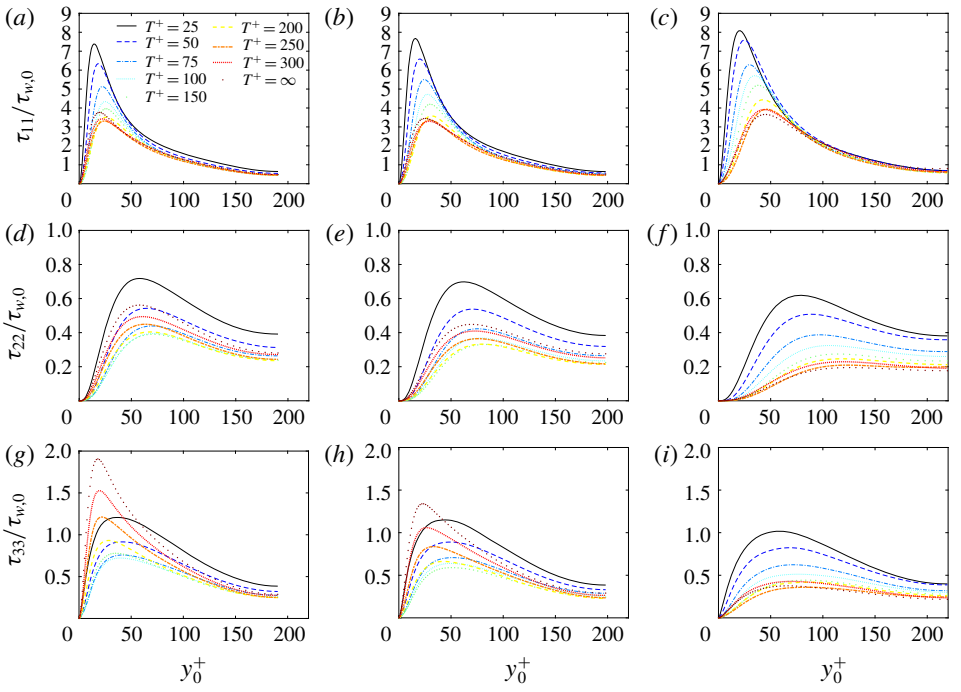


FIGURE 10. (Colour online) Reynolds normal stress components (normalized by the wall shear stress of the uncontrolled case $\tau_{w,0}$) as a function of y_0^+ for different oscillation periods T^+ at $A^+ = 12$ for (*a*,*d*,*g*) $M_b = 0.3$, (*b*,*e*,*h*) $M_b = 0.8$ and (*c*,*f*,*i*) $M_b = 1.5$. Rows (*a–c*), (*d–f*) and (*g–i*) correspond to τ_{11}, τ_{22} and τ_{33}, respectively.

turbulence is highly suppressed, but is significantly increased at large T^+. Structurally, SWO introduces a periodic realignment of the streak, whose tilting angle depends on the ratio between spanwise and streamwise velocity strain $(\mathrm{d}\langle w\rangle/\mathrm{d}y)/(\mathrm{d}\langle u\rangle/\mathrm{d}y)$, and the angle generally increases with T^+ due to increased spanwise strain. This realignment gives rise to a spanwise component of the velocity fluctuation in the inclined streak direction, and thus to an enhancement of τ_{33}. The near-wall peak decreases with increasing M_b and becomes less obvious for the $M_b = 1.5$ case. This is because the streamwise velocity strain $(\mathrm{d}\langle u\rangle/\mathrm{d}y)$ is much stronger at high M_b. Hence, the tilting angle and reorientation are also suppressed at high M_b for large T^+ – resulting in higher $\mathcal{DR}$.

Since the Reynolds shear stress τ_{12} is strongly linked to the skin-friction drag (Fukagata *et al.* 2002), figure 11 further examines τ_{12} profiles (normalized by the wall shear stress of the uncontrolled case $\tau_{w,0}$) in outer scaling. Similar to other Reynolds stress components, τ_{12} is substantially decreased under control, especially close to the wall, consistent with the fact that the peak also moves away from the wall. The decrease in the maximum value correlates with $\mathcal{DR}$. For example, the peak of τ_{12} at $T^+ = 300$ for $M_b = 1.5$ drops about 60 %, in absolute value, consistent with the decrease in total skin friction of around 45 % when contributions from other parts are included, like the laminar part, discussed later.

Based on the compressible flow version of the FIK identity derived by Gomez *et al.* (2009), the physical decomposition of the total skin friction can be expressed as

https://doi.org/10.1017/jfm.2019.727 Published online by Cambridge University Press

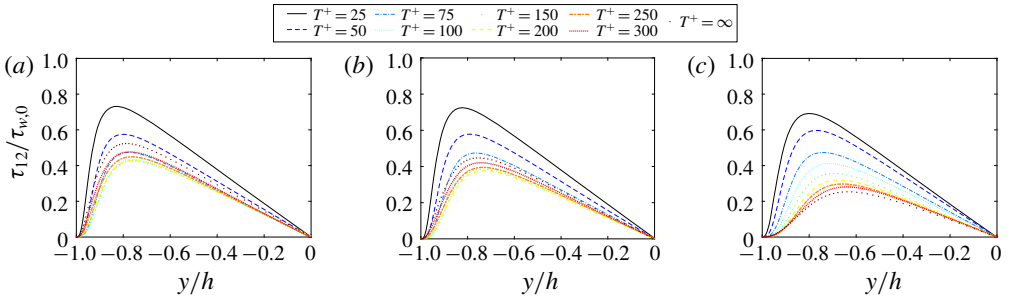


FIGURE 11. (Colour online) Reynolds shear stresses τ_{12} normalized by the wall shear stress of the uncontrolled case $\tau_{w,0}$ for different oscillation periods T^+ at $A^+ = 12$ for (*a*) $M_b = 0.3$, (*b*) $M_b = 0.8$ and (*c*) $M_b = 1.5$.

$$C_f = \underbrace{\frac{6}{Re_b}}_{C_f^L} + \underbrace{3\int_{-1}^{1} y\overline{\rho}\widetilde{u''v''}\,\mathrm{d}y}_{C_f^T} + \underbrace{\frac{3}{Re_b}\int_{-1}^{1} y\left(\frac{\overline{\mu}}{\overline{\mu}_w} - 1\right)\frac{\partial \overline{u}}{\partial y}\mathrm{d}y}_{C_f^\mu} + \underbrace{\frac{3}{Re_b}\int_{-1}^{1} y\overline{\mu'\left(\frac{\partial u'}{\partial y} + \frac{\partial v'}{\partial x}\right)}\,\mathrm{d}y}_{C_f^{\mu T}}, \tag{3.6}$$

which decomposes the skin friction into four components: an 'equivalent' laminar part C_f^L; a turbulent part C_f^T represented by the weighted integration of the total Reynolds shear stress; the compressible contribution C_f^μ related to the mean viscosity variations and the mean wall-normal velocity gradient; and the compressible–turbulent interaction part $C_f^{\mu T}$. Note that the latter two terms, absent for the strictly incompressible case, together contribute less than 0.3 % of the total skin friction for our nearly incompressible case (i.e. $M_b = 0.3$), hence are ignored in the following discussion. The weight in the integration decreases linearly with increasing distance from the wall, which clearly highlights the contribution of near-wall turbulent structures to the skin friction.

The decomposed total skin friction C_f (normalized by the uncontrolled case $C_{f,0}$) for different oscillation periods T^+ is depicted in figure 12 for different M_b cases. First, the compressible–turbulent interaction term $C_f^{\mu T}$ is negligible (less than 0.4 % for all cases). This is also confirmed by Zhe *et al.* (2016) even for an $M = 6$ hypersonic turbulent boundary layer. Since Re_b is fixed, C_f^L is held constant for all cases, which contributes approximately 25 % of the total C_f for the uncontrolled case. The compressible contribution term C_f^μ is also small, and increases as M_b increases, becoming 1.3 % at $M_b = 0.8$ and 4.5 % at $M_b = 1.5$. Hence, C_f^T is the dominant contribution for the total C_f (similar to the incompressible case), and its contribution gradually decreases as M_b increases, being 75.0 %, 73.5 % and 69.8 % at $M_b = 0.3$, 0.8 and 1.5, respectively.

Parenthetically, since the normalized skin friction $C_f/C_{f,0}$ is $1 - \mathcal{DR}$, its variation with respect to T^+ is just opposite to that for $\mathcal{DR}$ (figure 5*a*). Under control, C_f^μ is only slightly altered for the $M_b = 0.8$ case. For example, $C_f^\mu/C_{f,0}$ increases to approximately 1.8 % for $T^+ = 25$, the smallest oscillation period considered. The

https://doi.org/10.1017/jfm.2019.727 Published online by Cambridge University Press

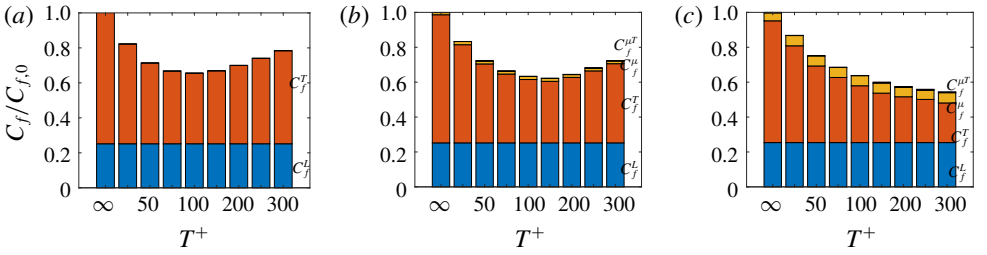


FIGURE 12. (Colour online) Decomposed skin friction C_f (normalized by the uncontrolled case $C_{f,0}$) for different oscillation periods T^+ at $A^+ = 12$ for (*a*) $M_b = 0.3$, (*b*) $M_b = 0.8$ and (*c*) $M_b = 1.5$. Note that $T^+ = \infty$ denotes the uncontrolled case.

slight alteration is understandable since the temperature (hence also viscosity) is only mildly altered by SWO for the subsonic cases. Besides, the integrand of C_f^{μ} is very small near the wall as $\overline{\mu}/\overline{\mu}_w - 1$ goes to zero near the wall. For the $M_b = 1.5$ case, the contribution of C_f^{μ} further increases, due to increased viscosity under SWO. In particular, the contribution of C_f^{μ} increases to approximately 6.0 % of the total $C_{f,0}$ at $T^+ = 25$, which partially explains why $\mathcal{DR}$ deteriorates at small T^+. For $M_b = 0.3$, the reduction in total C_f is only due to the decrease in C_f^T (corresponding to the suppression of the turbulent Reynolds shear stress). From figure 12, it is obvious that, even for the $M_b = 1.5$ case, the reduction in total C_f is also mainly due to the decrease in C_f^T.

3.6. *Energy spectrum*

Figure 13 compares the pre-multiplied spanwise spectrum of streamwise velocity $k_z E_{uu}$ (normalized by the maximum value of the uncontrolled case) as a function of spanwise wavelength λ_z^+ between the uncontrolled and controlled cases. Here, the near-optimal control period with $T^+ = 150$ is considered. The peak location of the spectrum, denoted as $+$ in the figure, typically represents the mean streak spacing. For incompressible flows, the near-wall streak spacing in the viscous sublayer is typically of the order of 10^2 wall units and remains remarkably constant over a wide range of Reynolds numbers (Lozano-Durán & Jiménez 2014). Figure 13 shows that the streak spacing increases with M_b when scaled in wall units. In particular, the wavelength increases from $\lambda_z^+ \approx 120$ for $M_b = 0.3$ to $\lambda_z^+ \approx 140$ for $M_b = 0.8$ and to $\lambda_z^+ \approx 175$ for $M_b = 1.5$. Also, the wall-normal location of the peak also increases as M_b increases, which is consistent with an outward shift of the streamwise Reynolds stress in figure 10. Compared with the uncontrolled case, the contribution from the near-wall region is effectively suppressed, especially at higher M_b, and the energy-containing part is also shifted outward with a much weaker peak. This suggests that the streaks under SWO are significantly weakened, which is further confirmed with the flow visualization shown below.

3.7. *Coherent structures*

The effect of control on near-wall coherent structures is examined. Figure 14 shows the top view of instantaneous vortical structures visualized using λ_ρ criterion (Yao & Hussain 2018) for both uncontrolled and controlled (for $T^+ = 150$) cases; also shown are the streaks at $y^+ \approx 15$. Note that the time selected for the controlled

https://doi.org/10.1017/jfm.2019.727 Published online by Cambridge University Press

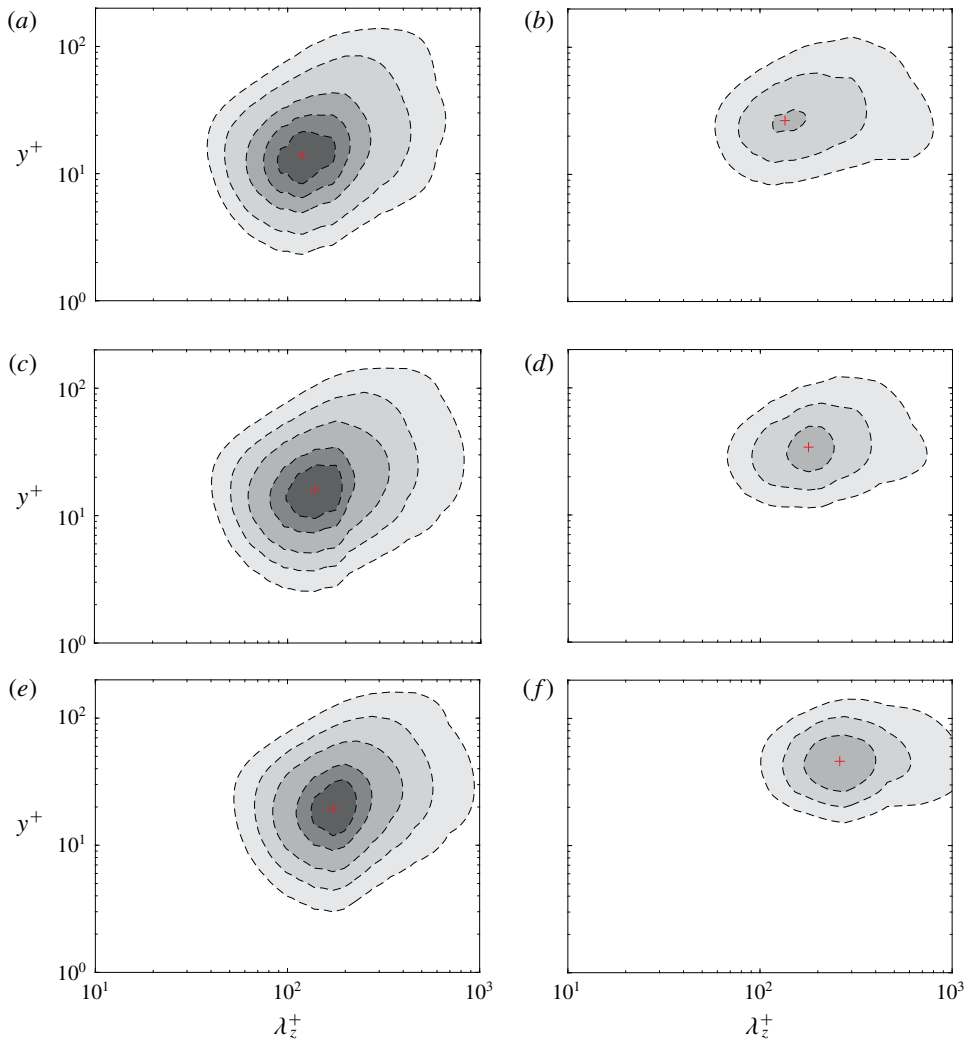


FIGURE 13. (Colour online) Pre-multiplied spanwise spectrum of streamwise velocity $k_z E_{uu}$ (normalized by the maximum value of uncontrolled case) as a function of λ_z^+ at $Re_b = 3000$ for (*a*,*b*) $M_b = 0.3$, (*c*,*d*) $M_b = 0.8$ and (*e*,*f*) $M_b = 1.5$. (*a*,*c*,*e*) Uncontrolled and (*b*,*d*,*f*) controlled cases with $A^+ = 12$ and $T^+ = 150$. The + symbol denotes the location of maximum value.

cases is around the same oscillation phase for all M_b cases. For the uncontrolled case at $M_b = 0.3$, typical meandering low-speed streak structures are observed aligned along the streamwise directions; and the streamwise vortices are mainly located near the interface of low- and high-speed streaks. As M_b increases, the streaks become more coherent (longer and less wavy), and hence more stable (Patel *et al.* 2016). Correspondingly, the streamwise vortices are more sparsely distributed and elongated. Similar observations have been reported by Coleman *et al.* (1995) for supersonic turbulent channel flow and by Duan *et al.* (2010) for supersonic turbulent boundary layers with cooled walls. Patel *et al.* (2016) showed that, for the $dRe_\tau^*/dy < 0$ case (typical of all flows considered in this paper), the inclining and tilting of the vortices

https://doi.org/10.1017/jfm.2019.727 Published online by Cambridge University Press

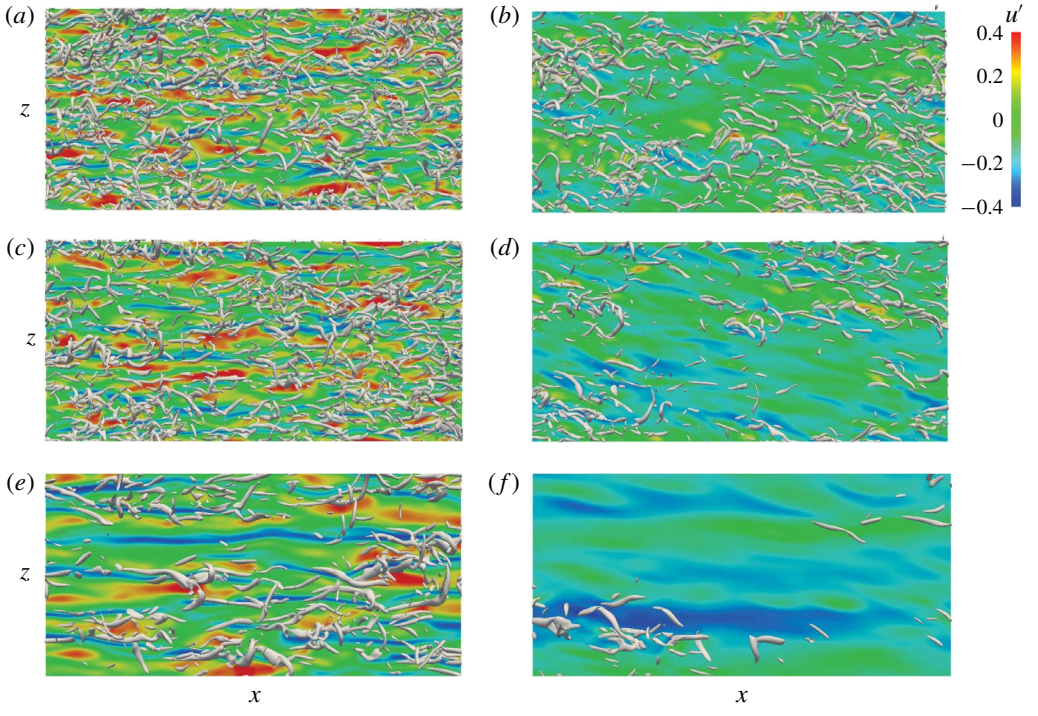


FIGURE 14. (Colour online) Top view of instantaneous vortical structures (visualized using λ_ρ^+) associated with the streamwise velocity fluctuations (streaks) $|u'/U_b| < 0.4$ at $y^+ \approx 15$ for $Re_b = 3000$ and $M_b =$ (*a*,*b*) 0.3, (*c*,*d*) 0.8 and (*e*,*f*) 1.5. (*a*,*c*,*e*) Uncontrolled and (*b*,*d*,*f*) controlled cases with $T^+ = 150$. The red (dark) and blue (light) correspond to positive and negative fluctuations. Note that the domain size is $L_x \times L_z = 6\pi h \times 2\pi h$.

decrease, and the streaks are more stabilized compared with the constant-property case.

Compared with the uncontrolled cases, the strength of the streaks is significantly weakened under control. Consequently, the generation of drag-inducing near-wall streamwise vortices is also suppressed, especially for the $M_b = 1.5$ case, where only a few vortices are observed. Besides, the streaks are tilted along the spanwise direction. This is similar to that reported in Touber & Leschziner (2012), where the near-wall streaks are periodically reoriented based on the phase of the oscillation – a consequence of the competing effect of the streamwise and spanwise velocity components. While the bulk flow tries to align the low-speed streaks in the streamwise direction, simultaneously a spanwise velocity component due to SWO tends to tilt the streak to the spanwise direction. Touber & Leschziner (2012) showed that the spanwise tilting angle of the streaks coincides with the angle of the mean shear $(\mathrm{d}\langle w\rangle/\mathrm{d}y)/(\mathrm{d}\langle u\rangle/\mathrm{d}y)$ around $y^+ = 10$. Using conditional averaging, Yakeno *et al.* (2014) also demonstrated that the spanwise tilting angle of the near-wall vortical structures could also be well estimated from the ratio between spanwise and streamwise strain shear. It would be interesting to investigate the impact of SWO on modification of streamwise vortices for the compressible cases.

The flow field difference among three different M_b cases is further examined through the velocity vectors in the cross-section (y–z) plane, along with the streamwise

https://doi.org/10.1017/jfm.2019.727 Published online by Cambridge University Press

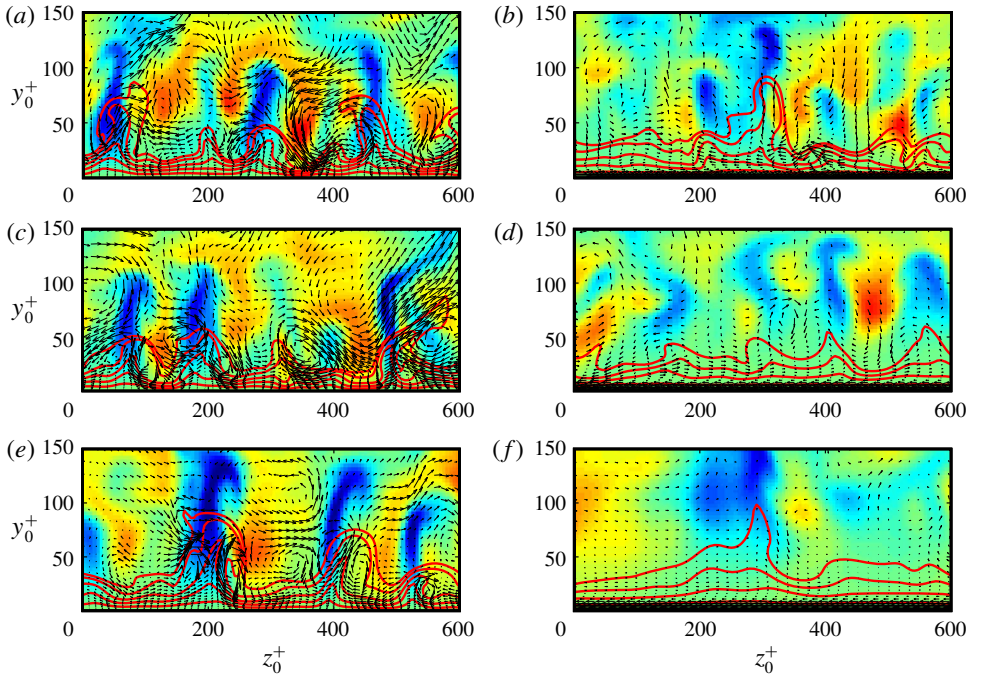


FIGURE 15. (Colour online) Vector plots of (v, w) in the cross-section $(y–z)$ plane located at $x = L_x/2$ in figure 14 for (a,b) $M_b = 0.3$, (c,d) $M_b = 0.8$ and (e,f) $M_b = 1.5$. (a,c,e) Uncontrolled and (b,d,f) controlled cases with $T^+ = 150$. The red (dark) and blue (light) correspond to positive and negative streamwise velocity fluctuations. The red lines represent the iso-contours of the streamwise velocity $u = [0.2\ 0.4\ 0.6\ 0.8]U_b$.

velocity fluctuations u', in figure 15. The near-wall quasi-streamwise vortices eject low-speed fluid away from the wall and sweep high-speed fluid towards the wall; note that the effects of shear stress decreasing ejection and shear stress increasing sweep events are unequal, the latter dominating, hence the net effect being increased skin friction by the vortices (Schoppa & Hussain 2002). The streak spacing continuously increases as M_b increases. For example, compared with five complete streaks identified in the region with a spanwise length of 600 wall units at $M_b = 0.3$, there are only three streaks at $M_b = 1.5$, which is qualitatively consistent with the mean streak spacing of $\lambda_z^+ \approx 175$ found from the pre-multiplied energy spectrum in figure 13. Morinishi *et al.* (2004) and Patel *et al.* (2015) also showed that the semi-local scaling could be sufficient to account for the changes in the scales of streak in the buffer layer, to be discussed in § 4.3. Additionally, the streak strength (typically quantified by the streak flank angle) is reduced by SWO. In other words, the streak becomes more stable for high M_b cases, which is reasonable since the streamwise vortices have more difficulty in ejecting fluid from the wall as both the density and viscosity increase near the wall. This is also consistent with the attenuation of wall-normal velocity fluctuations at higher M_b discussed in § 3.5. SWO significantly weakens the near-wall streaks. Not only the number of streaks but also the streak flank angle is decreased compared with the uncontrolled case. The weakening effect is enhanced as M_b increases since the near-wall density and viscosity are further increased due to SWO. In particular, only one complete streak is observed for the $M_b = 1.5$ case. The

https://doi.org/10.1017/jfm.2019.727 Published online by Cambridge University Press

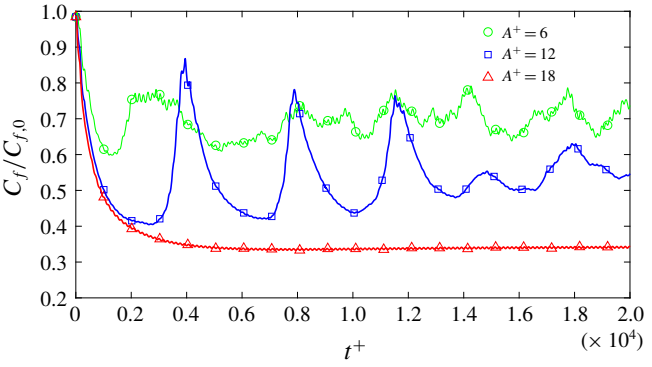


FIGURE 16. (Colour online) Time evolution of skin friction normalized by the uncontrolled case $C_f/C_{f,0}$ at $T^+ = 300$ and different A^+ for $Re_b = 3000$ and $M_b = 1.5$.

weakened streaks lead to the suppression of the generation of streamwise vortices through streak instability/transient growth (Schoppa & Hussain 2002) – resulting in drag reduction.

3.8. *Amplitude effect at* $Re_b = 3000$

To further examine the amplitude effect, additional DNS are performed at two other oscillation amplitudes $A^+ = 6$ and 18 for the $M_b = 1.5$ case. Figure 5(*b*) shows the drag reduction $\mathcal{DR}$ as a function of T^+ for different A^+ values. Consistent with the observations for incompressible flow (Quadrio & Ricco 2004), at given T^+, $\mathcal{DR}$ increases with A^+, but the rate of increase decreases as A^+ becomes large. Similar to the $A^+ = 12$ case, $\mathcal{DR}$ monotonically increases with T^+ at $A^+ = 18$, and changes rapidly at $T^+ = 300$, where the flow is relaminarized (evident from the time evolution of skin friction in figure 16). For the small-amplitude case $A^+ = 6$, $\mathcal{DR}$ exhibits the traditional non-monotonic variation with T^+, with $\mathcal{DR}_{max} = 33.9\,\% \pm 0.8\,\%$ obtained at $T^+ = 200$.

Figure 16 shows the long-time evolution of normalized skin friction $C_f/C_{f,0}$ at $T^+ = 300$. For the low-amplitude case $A^+ = 6$, skin friction exhibits similar behaviour to that shown previously: C_f reaches the low-drag state after transients and exhibits small fluctuations due to the turbulence response of wall actuation. For the $A^+ = 12$ case, C_f experiences large oscillation before slowly reaching a steady state. For the $A^+ = 18$ case, C_f slowly converges to a constant value without large fluctuation, which is about 33.6 % of $C_{f,0}$, suggesting that the flow is relaminarized. It is worth mentioning that a similar relaminarization was also observed for drag control using travelling wave-like wall deformation method (Nakanishi *et al.* 2012). The initial, periodic large C_f oscillations for the $A^+ = 12$ case and the complete relaminarization for $A^+ = 18$ case are quite surprising. As suggested by one referee, these might be due to the limited domain size effect. To address this issue, in the Appendix, we conduct additional simulations for these two cases by doubling the domain length and width. For $A^+ = 18$, the flow also relaminarizes for the doubled domain size case with identical C_f variation. However, for $A^+ = 12$, we do find an interesting difference: the initial transient period of large C_f oscillations becomes shorter, and C_f reaches a steady state earlier than for the smaller domain size case. These results seem to suggest that the domain sizes indeed have some influence on the flow transitional

https://doi.org/10.1017/jfm.2019.727 Published online by Cambridge University Press

behaviour (possibly also relaminarizaiton). Alternation of such large C_f oscillations due to domain size variation was also reported in stably stratified turbulent channel flows (Garg *et al.* 2000; Armenio & Sarkar 2002; Iida, Kasagi & Nagano 2002; Garcia-Villalba & Del Alamo 2011). Elaborate analysis needs to be carried out to fully understand the possible reasons for transition and relaminarization and the underlining flow physics, which is beyond the scope of this paper.

Interesting, even for the relaminarized case, C_f experiences periodic undulation, which is in contrast to the incompressible case, where C_f remains constant. To address this, phase-averaged Reynolds shear stress is examined. Combining the phase and Favre averaging, an instantaneous velocity can be expressed as

$$\phi = \check{\phi}(y, \tau) + \phi'''(x, y, z, t), \tag{3.7}$$

where $\check{\phi}$ is called phase Favre averaging with random fluctuation ϕ''' defined as

$$\check{\phi} = \langle \rho\phi \rangle / \langle \rho \rangle, \tag{3.8}$$

$$\phi''' = \phi - \check{\phi}. \tag{3.9}$$

The phase-Favre-averaged quantity is further decomposed into time-averaged and periodic components as follows:

$$\check{\phi}(y, \varphi) = \widetilde{\phi}(y) + \hat{\phi}(y, \varphi), \tag{3.10}$$

so that the instantaneous field can be written in the triple decomposed form as

$$\phi = \widetilde{\phi}(y) + \hat{\phi}(y, \varphi) + \phi'''(x, y, z, t), \tag{3.11}$$

with $\phi'' = \hat{\phi} + \phi'''$.

The phase-averaged Reynolds shear stress can be expressed as

$$\langle \rho u'' v'' \rangle = \langle \rho(\hat{u} + u''')(\hat{v} + v''') \rangle = \hat{u} \langle \rho v \rangle, \tag{3.12}$$

where $u''' = v''' = 0$ for laminar flow is used. For the incompressible case, based on continuity, $\langle \rho v \rangle \equiv 0$, hence $\langle \rho u'' v'' \rangle \equiv 0$. However, this is no longer valid for compressible flow. From the phase-averaged continuity equation, we have

$$\frac{\partial \langle \rho \rangle}{\partial t} + \frac{\partial \langle \rho v \rangle}{\partial y} = 0. \tag{3.13}$$

Due to the periodic variation of phase-averaged density $\langle \rho \rangle$, $\langle \rho v \rangle$ is no longer zero, so is $\langle \rho u'' v'' \rangle$.

Figure 17 shows, for the relaminarized case, the phase-averaged skin-friction distribution $\langle C_f \rangle$, along with $\langle \rho v \rangle$, Reynolds shear stress $\langle \rho u'' v'' \rangle$ and $\mathrm{d}\langle \rho w \rangle / \mathrm{d}y$ denoting the Stokes strain. The skin friction $\langle C_f \rangle$ varies within the cycling phase φ with the oscillation period of half the SWO period. Additionally, $\langle \rho v \rangle$ also varies with φ and with maximum variation located around $y/h = -0.9$. Consequently, the Reynolds shear stress $\langle \rho u'' v'' \rangle$ also varies periodically with φ. Consistent with the observation made in Touber & Leschziner (2012), figure 17 shows that the skin friction is also related to the Stokes strain: $\langle C_f \rangle$ rises when the Stokes strain near the wall is high while it decreases when the strain is low. Hence, due to the periodic variation of the thermodynamic quantities caused by SWO, even for the laminar

https://doi.org/10.1017/jfm.2019.727 Published online by Cambridge University Press

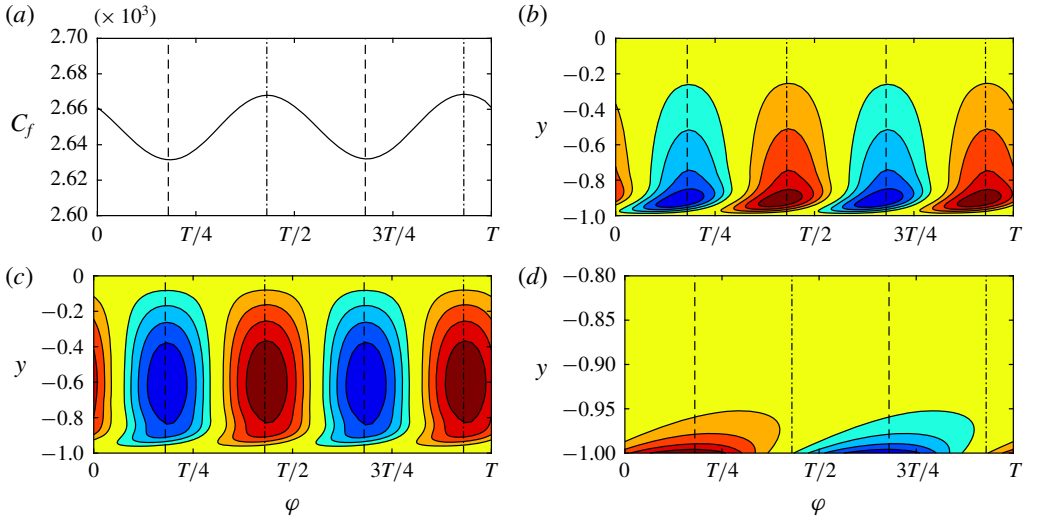


FIGURE 17. (Colour online) Comparison between (*a*) phase-wise averaged skin friction $\langle C_f \rangle$, (*b*) $\langle \rho v \rangle$, (*c*) $\langle \rho u'' v'' \rangle$ and (*d*) $\mathrm{d}\langle \rho w \rangle / \mathrm{d}y$ for the relaminarized case ($A^+ = 18$ and $T^+ = 300$) for $Re_b = 3000$ and $M_b = 1.5$. Dashed and dash-dotted vertical lines denote locations of the minimum and maximum of $\langle C_f \rangle$, respectively.

case the motions in the streamwise and spanwise directions are coupled. This is in contrast to the incompressible flow, where these two flows can be decoupled. The periodical variation of thermodynamic properties is also the reason why skin friction C_f experiences strong oscillations at small T^+ for the $M_b = 1.5$ case (figure 4*c*).

The decomposed total skin-friction drag for different T^+ is shown in figure 18. Again, C_f^T is the dominant term for the reduction of total C_f. For the relaminarized case ($A^+ = 18$ and $T^+ = 300$), the turbulence contribution C_f^T becomes zero. Not surprisingly, the existence of compressible part C_f^μ due to non-uniform thermodynamic properties causes the skin friction for the relaminarized compressible flow to be slightly higher than that for the well-known incompressible laminar cases. Due to increased viscosity near the wall caused by increased temperature, the compressible contribution C_f^μ continuously increases with A^+. For example, at $T^+ = 25$, $C_f^\mu / C_{f,0}$ markedly increases from approximately 4.9 % at $A^+ = 6$ to 8.1 % at $A^+ = 18$. This suggests that $\mathcal{DR}$ might be decreased at very high A^+, due to enhanced compressibility contribution C_f^μ. This is quite different from the incompressible case, where $\mathcal{DR}$ monotonically increases with A^+ (figure 5*b*; see also Quadrio & Ricco (2004)).

4. Further results: Reynolds number effects and comparison with incompressible cases

4.1. *Reynolds number effect*

Since the Reynolds number effect is an important issue for drag control, we performed additional studies at a higher $Re_b = 7667$ for the subsonic $M_b = 0.8$ and supersonic $M_b = 1.5$ cases (denoted as C8kM08 and C8kM15 cases, respectively). Figure 19 shows the initial time evolution of the normalized skin friction coefficient $C_f(t)/C_{f,0}$ for different oscillation periods T^+ with $A^+ = 12$ at $Re_b = 7667$. In general, the

https://doi.org/10.1017/jfm.2019.727 Published online by Cambridge University Press

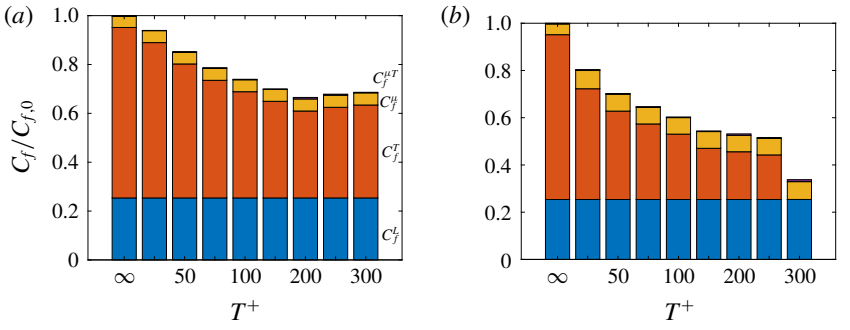


FIGURE 18. (Colour online) Decomposed skin friction C_f for different oscillating period T^+ at (*a*) $A^+ = 6$ and (*b*) $A^+ = 18$ for $Re_b = 3000$ and $M_b = 1.5$.

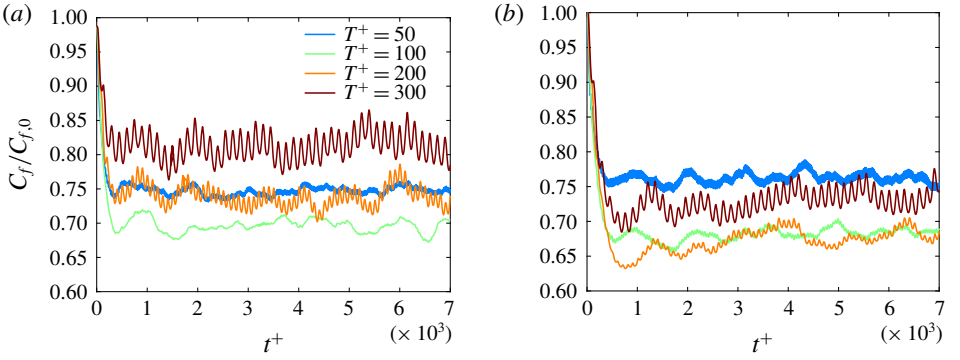


FIGURE 19. (Colour online) Initial time evolution ($t^+ \leqslant 7000$) of skin friction normalized by the uncontrolled case $C_f/C_{f,0}$ at different wall oscillation periods T^+ with $A^+ = 12$ for $Re_b = 7667$ and (*a*) $M_b = 0.8$ and (*b*) $M_b = 1.5$.

evolution of $C_f(t)$ has a similar pattern to that at $Re_b = 3000$ (figure 4), namely $C_f(t)$ initially rapidly decreases as the oscillation starts, then reaches a temporal minimum before approaching the statistically quasi-steady, low-drag state. However, compared with the results at $Re_b = 3000$, the long-time-scale undulation of C_f is suppressed, especially for the large T^+ cases. This suggests that the rapid increase and decrease of C_f for $Re_b = 3000$ and $M_b = 1.5$ might be due to a low Reynolds number effect. In addition, at the same T^+, the level of small-scale oscillation in C_f (indicating the flow responses to wall oscillation) is found to increase as Re_b increases, akin to the observation of Hurst *et al.* (2014) for the strictly incompressible case.

Figures 20(*a*) and 20(*b*) show $\mathcal{DR}$ as a function of T^+ at $A^+ = 12$ at two different Re_b values for the $M_b = 0.8$ and 1.5 cases, respectively. It can be seen that $\mathcal{DR}$ clearly decreases at higher Re_b, akin to the incompressible drag control using SWO (Gatti & Quadrio 2016; Hurst *et al.* 2014) as well as many other drag methods (Wang, Huang & Xu 2016; Yao, Chen & Hussain 2018). The rate of decrease strongly depends on the oscillation period T^+: $\mathcal{DR}$ changes less at small T^+ (large ω^+), but much more at large T^+. If assuming that drag reduction decreases with Reynolds number following $\mathcal{DR} \propto Re_\tau^{-\gamma}$, the scaling exponent γ for the $M_b = 0.8$ case increases from 0.1 for $T^+ = 25$ to 0.49 for $T^+ = 300$ (a large γ denotes a rapid decrease in $\mathcal{DR}$ with increasing Reynolds number). In particular, $\mathcal{DR}$ at $T^+ = 150$ has been reduced

https://doi.org/10.1017/jfm.2019.727 Published online by Cambridge University Press

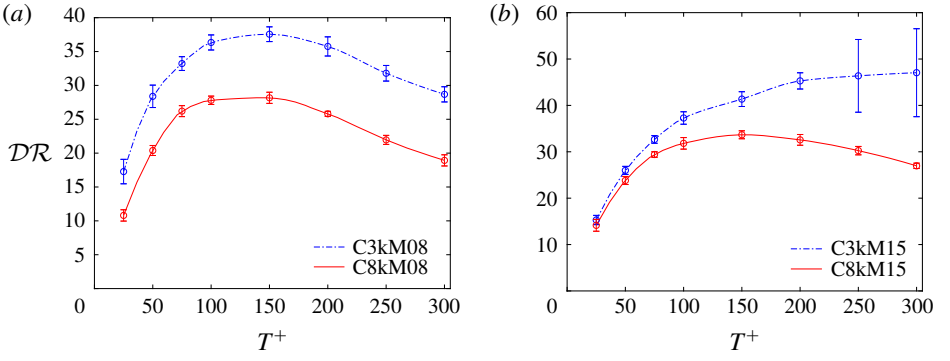


FIGURE 20. (Colour online) Reynolds number dependence of drag reduction $\mathcal{DR}$ versus oscillation period T^+ at $A^+ = 12$ for (*a*) $M_b = 0.8$ and (*b*) $M_b = 1.5$. The error bars indicate the corresponding uncertainty of $\mathcal{DR}$.

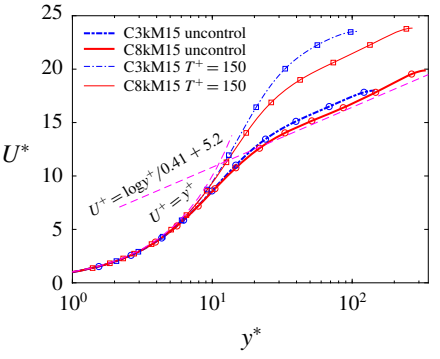


FIGURE 21. (Colour online) Comparison of Trettel–Larsson transformed mean streamwise velocity U^* as a function of y^* between uncontrolled and controlled at $T^+ = 150$ for C3kM15 and C8kM15 cases.

from $37.6\,\% \pm 1.1\,\%$ to $29.3\,\% \pm 1.1\,\%$, which corresponds to $\gamma = 0.29$ (close to the value of 0.35 obtained by Yao *et al.* (2019) for the incompressible case at the same T^+). Consistent with the finding for incompressible flow (Hurst *et al.* 2014; Yao *et al.* 2019), the optimal period T^+ also seems to decrease with increasing Re_b, i.e. from $T^+_{opt} = 150$ at $Re_b = 3000$ to $T^+_{opt} = 100$ at $Re_b = 7667$ (with $\mathcal{DR}_{max} = 30.3\,\% \pm 0.8\,\%$). For $M_b = 1.5$, $\mathcal{DR}$ becomes non-monotonically changing with T^+ at $Re_b = 7667$, with $\mathcal{DR}_{max}$ of $33.7\,\% \pm 0.6\,\%$ obtained at $T^+ = 150$. Figure 20(*b*) shows that the decrease in $\mathcal{DR}$ with Reynolds number is more severe for $M_b = 1.5$. However, recall that the drag control at $Re_b = 3000$ suffers from the low Reynolds number effect, where the flow does not remain fully developed at large T^+. Hence, inferring any Reynolds number scaling from those two cases can be limiting.

Flow statistics for $M_b = 1.5$ are compared between two different Re_b cases at the near-optimal control period (i.e. $T^+ = 150$). The mean velocity profiles using Trettel–Larsson transformation (U^*) are displayed in figure 21 for both uncontrolled and controlled cases at $M_b = 1.5$ with $Re_b = 3000$ and $Re_b = 7667$. For the uncontrolled case, the Trettel–Larsson transformed mean velocity profiles agree with the log-law profile, especially for the $Re_b = 7667$ case. When scaled with the actual friction

https://doi.org/10.1017/jfm.2019.727 Published online by Cambridge University Press

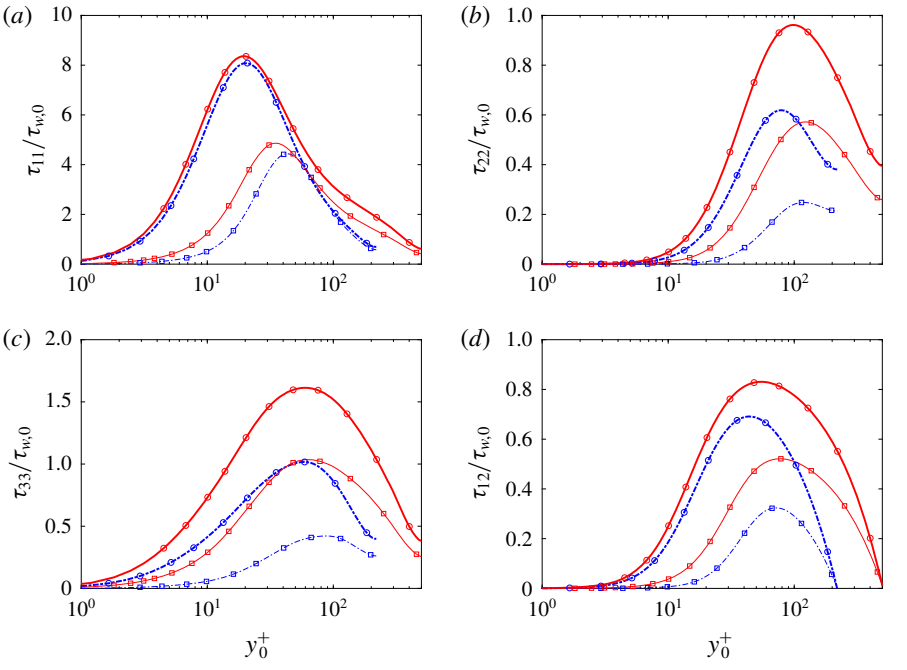


FIGURE 22. (Colour online) Comparison of Reynolds stress τ_{ij} profiles between uncontrolled and controlled at $T^+ = 150$ for C3kM15 and C8kM15 cases: (*a*) τ_{11}, (*b*) τ_{22}, (*c*) τ_{33} and (*d*) τ_{12}. See figure 21 for description of the curves.

velocity, the mean velocity profiles for the controlled flow collapse with those of uncontrolled cases in the viscous sublayer and are shifted upward in the log region. The shift decreases as Re_b increases, which is consistent with the findings for incompressible flows (Hurst *et al.* 2014; Yao *et al.* 2019). Gatti & Quadrio (2016) proposed a model to characterize $\mathcal{DR}$ via the vertical shift of the mean velocity profile. By further assuming that the upward shift would become invariant at high Re, they further employed this model to predict the possible amount of $\mathcal{DR}$ at practical Reynolds numbers. If this assumption is also valid for the compressible cases, it might be interesting to extend that to include the M_b effect, with the aid of certain mean velocity transformations, like van Driest or Trettel–Larsson transformations.

Figure 22 further shows the Reynolds stresses (τ_{11}, τ_{22}, τ_{33} and τ_{12}) at $Re_b = 3000$ and 7667 for $M_b = 1.5$. In general, all Reynolds stresses are significantly suppressed under SWO, and the location for the peak moves away from the wall. The decreases are much more substantial at lower Re_b. As Re_b increases, the effects of control on the Reynolds stresses become weaker. Taking τ_{11} for example, the maximum peak slightly increases for the uncontrolled case when Re_b increases from 3000 to 7667, but the difference between the two peaks becomes larger under control. In addition, the difference between the peak locations of the uncontrolled and controlled cases also decreases with increasing Re_b. All these findings show that SWO becomes less effective in suppressing turbulent fluctuations as Re_b increases, which explains why $\mathcal{DR}$ deteriorates at high Reynolds numbers (also valid for incompressible cases).

Figure 23 compares the pre-multiplied spanwise wavenumber spectrum of streamwise velocity $k_z E_{uu}$ (normalized by the maximum value of uncontrolled case) for

https://doi.org/10.1017/jfm.2019.727 Published online by Cambridge University Press

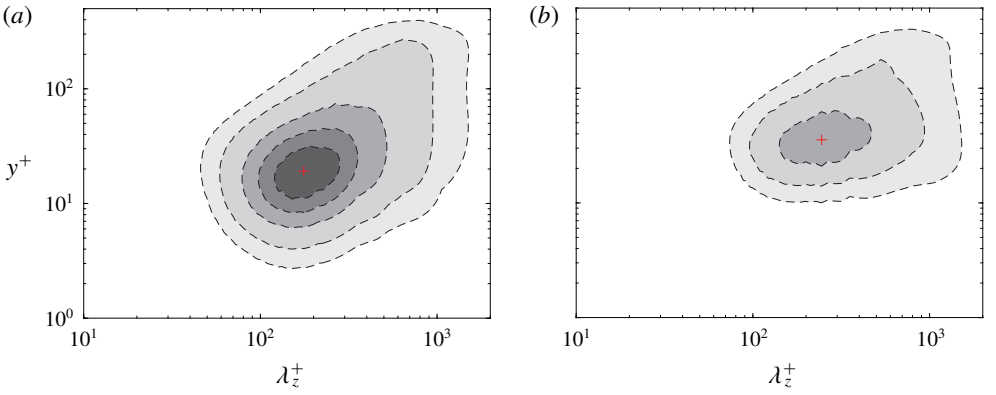


FIGURE 23. (Colour online) Pre-multiplied spanwise spectrum of streamwise velocity $k_z E_{uu}$ (normalized by the maximum value of uncontrolled case) as a function of λ_z^+ for C8kM15 for (*a*) uncontrolled and (*b*) controlled cases with $T^+ = 150$.

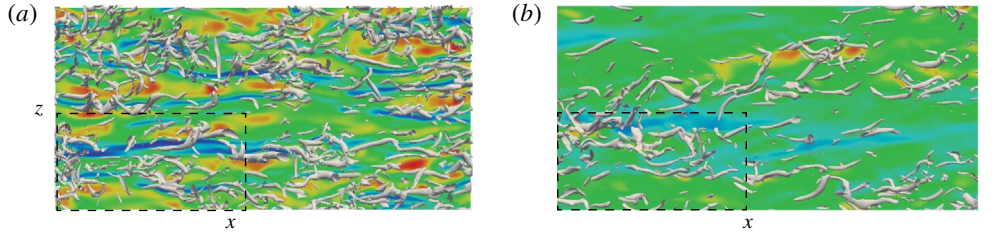


FIGURE 24. (Colour online) Top view of instantaneous vortical structures (visualized using λ_ρ^+) associated with the streamwise velocity fluctuations (streaks) $|u'/U_b| < 0.4$ at $y^+ \approx 15$ at C8kM15 for (*a*) uncontrolled and (*b*) controlled cases with $T^+ = 150$. The red (dark) and blue (light) correspond to positive and negative fluctuations. Note that the domain size is $L_x \times L_z = 6\pi h \times 2\pi h$, and the black dashed box corresponds to the same domain size as in figure 14 in wall units.

both uncontrolled and controlled cases with $T^+ = 150$. Compared with $Re_b = 3000$, the energy-containing part enlarges as Re_b increases. However, the peak location only varies slightly compared with the $Re_b = 3000$ case, which becomes $\lambda_z^+ \approx 179$ at $y^+ \approx 19.2$. Similar to the low Re_b cases, the intensity becomes weaker under control and the wall-normal location of the peak increases. However, compared with that at $Re_b = 3000$ (figure 13*f*), $k_z E_{uu}$ becomes less attenuated near the wall (i.e. $y^+ \lesssim 20$), suggesting less effectiveness of control.

The instantaneous vortical structures visualized using λ_ρ criterion, along with the streaks at $y^+ \approx 15$, are shown in figure 24 for both the uncontrolled and controlled cases for $Re_b = 7667$ and $M_b = 1.5$. Note that the black box in figure 24 indicates the same domain size as in figure 14(*e*,*f*) in wall units. For the uncontrolled case, vortices are clustered in the region of large-scale low-speed streaks. Although both the low-speed streaks and the near-wall streamwise vortices are suppressed under control, the suppression becomes less effective compared with the cases at $Re_b = 3000$. Figure 25 further displays the velocity vectors in the cross-section (y–z) plane at the middle of the streamwise domain, along with the streamwise velocity fluctuations u'. At the flank of the low-speed streak, several near-wall quasi-streamwise vortices

https://doi.org/10.1017/jfm.2019.727 Published online by Cambridge University Press

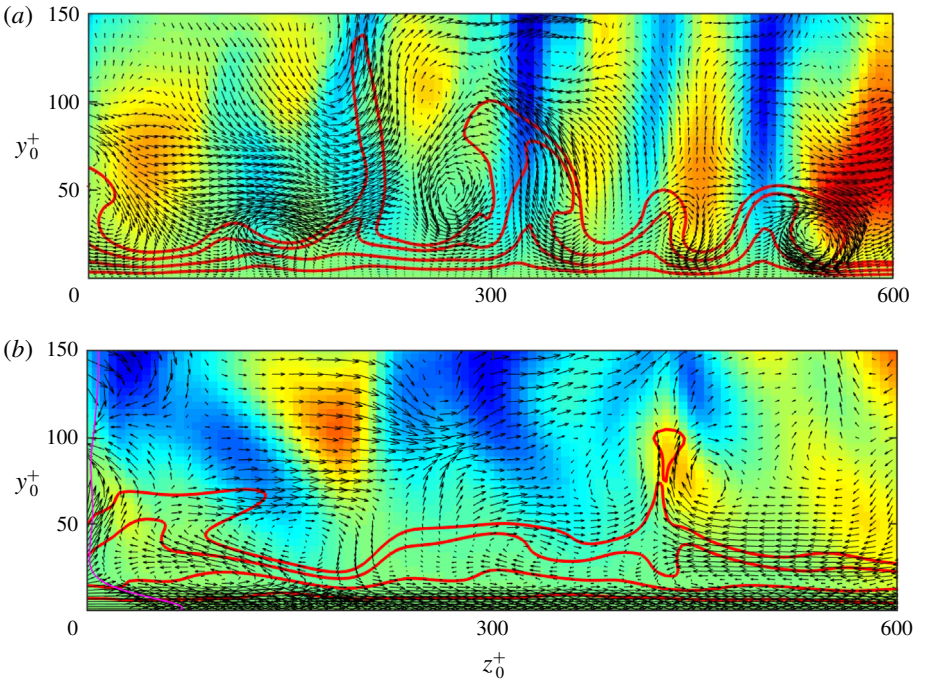


FIGURE 25. (Colour online) Vector plots of (v, w) in the y–z plane located at $x = L_x/2$ in figure 24 for C8kM15 case. (*a*) Uncontrolled and (*b*) controlled cases at $T^+ = 150$. The red (dark) and blue (light) correspond to positive and negative streamwise velocity fluctuations. The red lines represent the iso-contours of the streamwise velocity $u = [0.2\ 0.4\ 0.6\ 0.8]U_b$.

exist, ejecting/sweeping low-/high-speed fluid from/to the wall. Compared with those at $Re_b = 3000$ (figure 14*e*), these vortices becomes stronger. Under control, the streak becomes significantly weakened, especially very close to the wall. Interestingly, at this particular streamwise location, we capture one event of streak break up, which is caused by the squeezing and ejection motions of counter-rotating vortex pairs.

4.2. *Comparison with incompressible case at comparable semi-local Reynolds number*

Previous work on CTCF revealed that semi-local scaling can be employed to derive transformations that better collapse the mean velocity and turbulent statistics between incompressible and compressible cases (Huang *et al.* 1995; Modesti & Pirozzoli 2016; Patel *et al.* 2016). Figure 26 shows the mean velocity profiles using the Trettel–Larsson transformation and the Reynolds stresses as a function of y^* for two different Re_b values at $M_b = 1.5$. Two incompressible cases at matching $Re^*_{\tau c}$, namely 140 and 340, are also included for comparison. (Here, $Re^*_{\tau c}$ indicates the semi-local Reynolds number Re^*_τ at the half-channel centre height.) Clearly, the transformed mean velocity profiles are in good congruence with the incompressible cases. In addition, the semi-local scaling also yields good collapses for the Reynolds stresses. In particular, the wall-normal, spanwise and shear stresses are almost perfectly matched, and the peak locations of streamwise Reynolds stress occur at similar y^*, i.e. around 15. The only apparent difference is that the peak of the streamwise

https://doi.org/10.1017/jfm.2019.727 Published online by Cambridge University Press

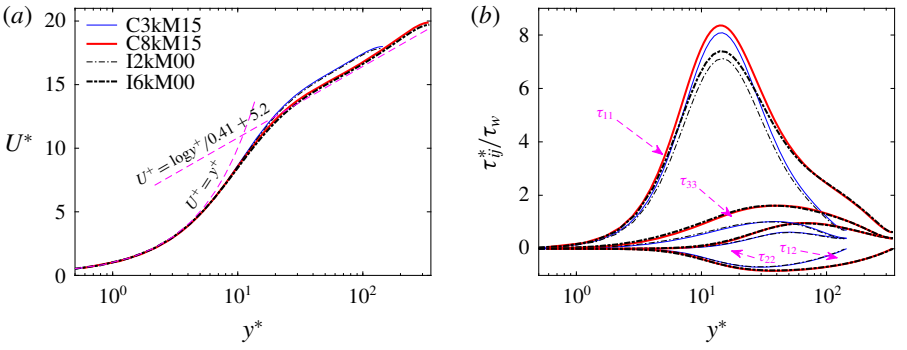


FIGURE 26. (Colour online) (*a*) Trettel–Larsson transformed mean velocity and (*b*) Reynolds stresses for the compressible C3kM15 and C8kM15 cases, along with the strictly incompressible cases at $Re_\tau = 140$ and 340.

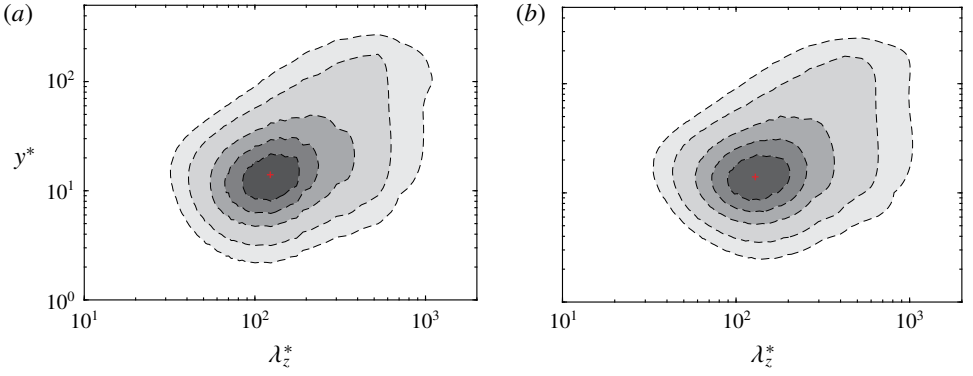


FIGURE 27. (Colour online) Pre-multiplied spanwise spectrum of streamwise velocity $k_z E_{uu}$ (normalized by the maximum value of uncontrolled case) in semi-local units for (*a*) C6kM00 and (*b*) C8kM15 cases.

Reynolds stress is slightly larger for the supersonic cases. Patel *et al.* (2015) found that the enhancement of the peak is related to the strengthening of the large-scale components of the streamwise velocity in the buffer layer.

Figure 27 further compares the pre-multiplied spanwise spectrum of streamwise velocity $k_z E_{uu}$ for the supersonic ($Re_b = 7667$ and $M_b = 1.5$) and the incompressible $Re_\tau = 340$ cases in semi-local units. Compared with figure 23(*a*), which shows the same quantity in wall units, the pre-multiplied spanwise spectrum of streamwise velocity in semi-local units better resembles that of the incompressible $Re_\tau = 340$ case. The mean-streak spacing, indicated by the peak location, becomes $\lambda^*_z \approx 120$ at $y^* = 15$, which is the same as for the incompressible case. Figure 28 further shows the instantaneous streamwise velocity fluctuations in the x–z plane at $y^* = 15$ for these two cases. For the supersonic case, representations in both classical wall units ($x^+ = xRe_\tau$) and semi-local units ($x^* = xRe^*_\tau$) are shown. The box size in streamwise and spanwise directions is 4000×2000, based on corresponding non-dimensional coordinates $x^+ \times z^+/x^* \times z^*$. In order to outline the physical scale of the structures, the black box in figure 28(*c*) indicates the domain of figure 28(*b*). Similar to the previous findings, the streaks become longer and sparse in wall units. However, when

https://doi.org/10.1017/jfm.2019.727 Published online by Cambridge University Press

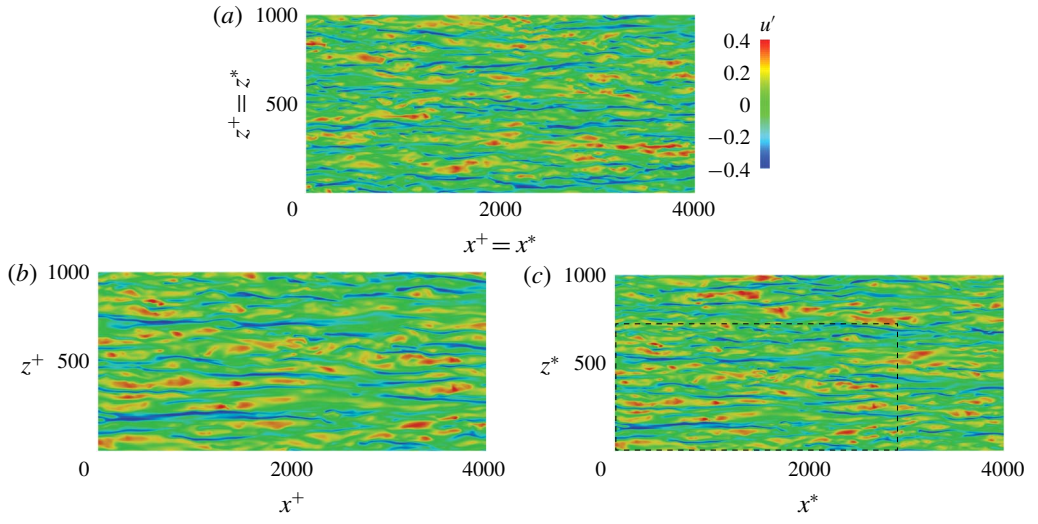


FIGURE 28. (Colour online) Instantaneous streamwise velocity fluctuations in the x–z plane at $y^* = 15$ for (*a*) I6kM00 case, (*b*) C8kM15 case using x^+–z^+ coordinates and (*c*) C8kM15 case using x^*–z^* coordinates. Note that the black box in (*c*) corresponds to (*b*).

scaled in the same local units, mean spanwise spacing and length of the streaks become similar between the supersonic and incompressible cases. Patel *et al.* (2016) also showed that the mean streak spacing, when scaled in semi-local units, is nearly universal for $y^* > 12$. Chen *et al.* (2014) also found that the wall-normal location of the induced vorticity–velocity correlation structures is quite universal in semi-local units for different M_b values.

All the above results demonstrate that there is a strong similarity between compressible and incompressible flows at matching $Re^*_{\tau c}$. Hence, it is interesting to investigate and compare drag control performance at comparable $Re^*_{\tau c}$. Figure 29(*a*) compares $\mathcal{DR}$ as a function of T^+ at $A^+ = 12$ between the supersonic $M_b = 1.5$ (with $Re_b = 3000$ and 7667) and the incompressible ($Re_\tau = 140$ and 340) cases. Similar to figure 5, the optimal oscillation period T^+_{opt} becomes large for the supersonic cases. Based on our observation that the length scale increases with M_b when scaled in wall units and can match well when scaled in semi-local units, we propose a simple transformation to better collapse $\mathcal{DR}$ between incompressible and compressible cases. For a given oscillation period T^+ and amplitude A^+, the control can also be described by another parameter, namely its maximum displacement D, which is $D = AT/\pi$ for the sinusoidal oscillation case. Now, let us assume that at the same $Re^*_{\tau c}$, the length scale of the forcing is correlated with the mean streak spacing of the flow, then we have

$$\frac{D^*}{l^*} = \frac{D^+_I}{l^+_I} = \frac{D^+_C}{l^+_C}, \tag{4.1}$$

where I and C denote the length scale for the incompressible and compressible cases, respectively, and l^* and D^* are the normalized length scale for the streak and control. Moreover, we have $l^* = l^+_I$. For the same oscillation amplitude A^+, we can obtain a normalized oscillation period as

$$T^* = T^+_I = T^+_C \frac{l^+_I}{l^+_C}. \tag{4.2}$$

https://doi.org/10.1017/jfm.2019.727 Published online by Cambridge University Press

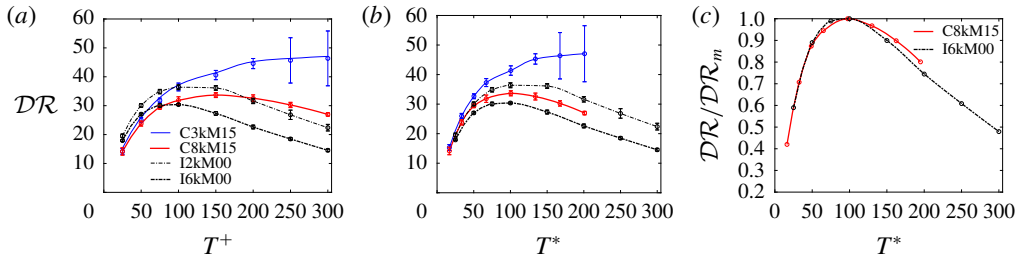


FIGURE 29. (Colour online) Comparison of $\mathcal{DR}$ (%) for different cases (C3kM15, C8kM15, I2kM00 and I6kM00) at $A^+ = 12$ as a function of (*a*) T^+ and (*b*) T^*. (*c*) Values of $\mathcal{DR}$ normalized by the maximum as a function of T^* for C8kM15 and I6kM00 cases. The error bars in (*a*,*b*) indicate the corresponding uncertainty of $\mathcal{DR}$.

Figure 29(*b*) shows $\mathcal{DR}$ as a function of T^* for supersonic and incompressible cases. Compared with figure 29(*a*), $\mathcal{DR}$ agrees better between these cases, except that $\mathcal{DR}$ is slightly higher for the supersonic case – this seems understandable since the streaks are more coherent and stable in the supersonic case. This is even true for flow under SWO, where the density and viscosity are further increased near the wall. Figure 29(*c*) further shows $\mathcal{DR}$ normalized by the maximum value for the supersonic $M_b = 1.5$ with $Re_b = 7667$ and incompressible $Re_\tau = 340$ cases (note that due to monotonic increase for the $Re_b = 3000$ case, the two low-Reynolds-number cases are not included for comparison). Clearly, $\mathcal{DR}$ shows a better collapse, especially at small T^*. The optimal T^*_{opt}, which is around 100, seems to be M_b-invariant.

Figure 30(*a*,*b*) compares the mean velocity U^* and Reynolds shear stress τ_{12} between the supersonic $Re_b = 7677$ and incompressible $Re_\tau = 340$ cases near T^*_{opt} (corresponding to $T^+ = 100$ for the incompressible $Re_\tau = 340$ and $T^+ = 150$ for the supersonic $Re_b = 7677$ cases, respectively). Except for a slightly larger upward shift associated with higher $\mathcal{DR}$, the mean velocity profiles under control are well collapsed between these two cases. In addition, the Reynolds shear stress also shows good congruence. Figure 30(*c*) further shows decomposed skin friction C_f for these two different cases. For the incompressible, uncontrolled case, the decomposition only contains laminar C_f^L and turbulent contributions C_f^T, amounting to about 15.1 % and 84.9 %, respectively. Under control, the turbulent contribution C_f^T decreases to approximately 54.7 %. For the supersonic case, the laminar C_f^L and compressible C_f^μ parts contribute about 12.2 % and 2.1 %, respectively, and the turbulent contribution C_f^T is approximately 85.5 %. Under control, the compressible part C_f^μ increases by approximately 0.3 %, while the turbulent part C_f^T decreases to about 51.6 % of $C_{f,0}$, resulting in a total 3.3 % more $\mathcal{DR}$ for the supersonic case. It is also worth mentioning that as Re_b increases, the contributions from laminar C_f^L and compressible C_f^μ parts decrease, and that from the turbulent part C_f^T monotonically increases, which suggests that at high Reynolds numbers the suppression of the turbulent Reynolds shear stress is still the primary objective of drag control for supersonic flows.

The response of the motions at different scales to the control is further discussed with the pre-multiplied wavenumber spectrum of the Reynolds stresses. Figure 31(*a*) compares the pre-multiplied spanwise wavenumber spectrum of the streamwise Reynolds stress $k_z E_{uu}/u_\tau^2$ as a function of wavelength λ_z^* at $y^* = 15$ for the above cases. As discussed, the spectrum for the uncontrolled case displays a distinct peak, approximately located at $\lambda_z^* \approx 120$ and is almost invariant with M_b. Compared

https://doi.org/10.1017/jfm.2019.727 Published online by Cambridge University Press

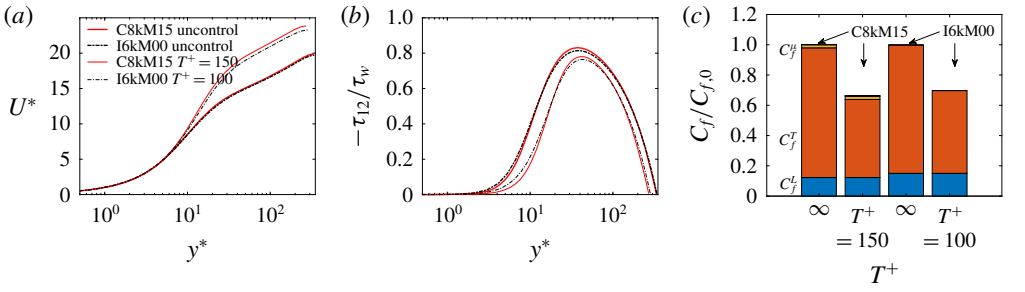


FIGURE 30. (Colour online) Comparison of (*a*) Trettel–Larsson transformed mean velocity U^*, (*b*) Reynolds shear stress τ_{12} and (*c*) decomposed skin friction C_f between uncontrolled and near-optimal controlled cases for C8kM15 and I6kM00.

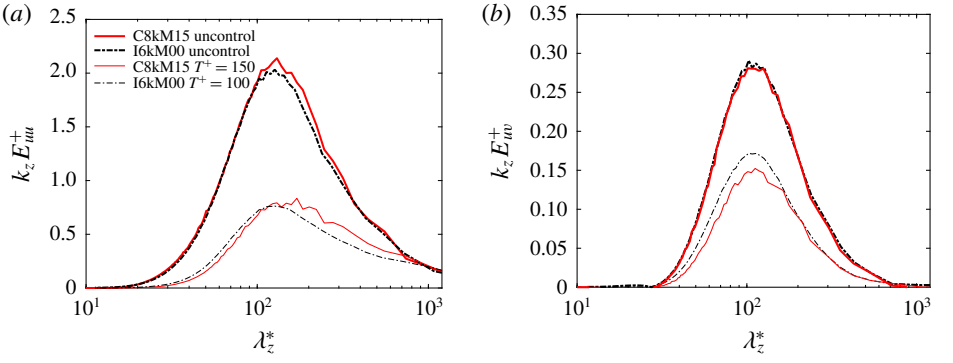


FIGURE 31. (Colour online) Comparison of pre-multiplied spanwise spectra between uncontrolled and near-optimal controlled cases for C8kM15 and I6kM00 for (*a*) streamwise Reynolds stress $k_z E_{uu}/u_\tau^2$ and (*b*) Reynolds shear stress $k_z E_{uv}/u_\tau^2$ as a function of λ_z^* at the peak wall-normal locations $y^* \approx 15$ and 25, respectively.

with the incompressible case, the near-wall large scales are slightly larger for the supersonic case, causing a larger peak of the streamwise Reynolds stress (figure 26*b*). Under control, the overall shape of the spectrum is not significantly changed. The Reynolds stress is substantially suppressed at small scales, with the peak reduced to approximately 65 % of the uncontrolled value. For the supersonic case, the large-scale components are less suppressed compared with the incompressible case, indicating the presence of more large-scale streaks. Figure 31(*b*) further compares the pre-multiplied spanwise wavenumber spectrum of the Reynolds shear stress $k_z E_{uv}$ as a function of wavelength λ_z^* at $y^* = 25$. For the uncontrolled cases, the profiles are almost collapsed with a peak around $\lambda_z^* \approx 100$, which is also consistent with the finding in figure 26(*b*), where the Reynolds shear stress is better matched between the two cases. Here SWO significantly suppresses the stress at all scales. For the incompressible case, the peak under control is decreased to about 61 % of the uncontrolled one. For the supersonic case, a slightly larger suppression is observed, especially for the small scales (i.e. $\lambda_z^* < 200$), which, in combination of the above FIK analysis, suggests that the slightly higher $\mathcal{DR}$ for the supersonic case is due to enhanced effectiveness of suppressing near-wall turbulence.

https://doi.org/10.1017/jfm.2019.727 Published online by Cambridge University Press

5. Concluding remarks

Inspired by the large of amount of drag reduction achieved through SWO in incompressible flows, we performed a detailed study of the control effect on CTCF up to $Re_b = 7667$ and $M_b = 1.5$ by means of DNS.

The drag control performance is first investigated at a fixed bulk Reynolds number Re_b of 3000 for three different bulk Mach numbers: $M_b = 0.3$, 0.8 and 1.5 cases. The $\mathcal{DR}$ for the $M_b = 0.3$ case agrees with strictly incompressible results at equivalent Re_τ (Touber & Leschziner 2012; Gatti & Quadrio 2013; Hurst *et al.* 2014; Yao *et al.* 2019). At $M_b = 0.8$, $\mathcal{DR}$ has a similar trend to that of the $M_b = 0.3$ case, namely $\mathcal{DR}$ non-monotonically varies with T^+. Compared with the $M_b = 0.3$ case, $\mathcal{DR}$ slightly decreases at small T^+ but increases at large T^+. Consequently, the optimal oscillation period T^+_{opt} shifts to a larger value, i.e. 150. At $M_b = 1.5$, $\mathcal{DR}$ further decreases at small T^+ but, interestingly, increases monotonically with T^+.

To understand the underlying physical mechanism of drag reduction, detailed flow statistics and dynamics of the structures are examined. The phase-averaged spanwise velocity concurs with the incompressible laminar Stokes layer solution at small y^+ even for the $M_b = 1.5$ case, but progressively deviates from it as y^+ increases, and the deviation increases with M_b. The mean streamwise velocity is also examined using both van Driest and Trettel–Larsson transformations, where the latter is found to be better in collapsing with the incompressible case. The SWO results in a thickening of the viscous layer and upward shifting of the log layer, where the upward shift value is well correlated with $\mathcal{DR}$. The intensities of most Reynolds stresses are suppressed under control, and the peak locations also move outward. However, the spanwise Reynolds stress for the $M_b = 0.3$ case develops a near-wall peak at large T^+ when $\mathcal{DR}$ deteriorates. The formation of the near-wall peak is due to the periodic realignment of the streak caused by the SWO, whose angle depends on the relative strength between spanwise and streamwise strain $(\mathrm{d}\langle w\rangle/\mathrm{d}y)/(\mathrm{d}\langle u\rangle/\mathrm{d}y)$. The near-wall peak becomes less distinct at higher M_b, since the streamwise strain becomes stronger – partially explaining why $\mathcal{DR}$ at large T^+ behaves differently for different M_b values. The dynamical decomposition of drag using the compressible version of the FIK identity (Gomez *et al.* 2009) reveals that the primary contribution for $\mathcal{DR}$ is still the reduction of the turbulent part C_f^T through the suppression of random Reynolds shear stress. Besides, we found that the decreased $\mathcal{DR}$ at small T^+ for large M_b is due to increased contribution of the compressible part C_f^μ since the temperature (hence also viscosity) is significantly increased by the viscous dissipation of the Stokes layer.

Additional DNSs with $A^+ = 6$ and 18 are performed for the supersonic $M_b = 1.5$ case to evaluate the amplitude effect of the control. Consistent with the incompressible case, $\mathcal{DR}$ increases with A^+, but the rate of increase decreases at larger A^+. Interestingly, for $A^+ = 18$, flow is relaminarized (inferred from smooth skin friction C_f variation) at $T^+ = 300$. The initial, periodic large C_f oscillations for the $A^+ = 12$ case and the complete relaminarization for the $A^+ = 18$ case are quite surprising. To explore the possible reason due to the domain size effect as reported in stably stratified turbulent channel flows (Garg *et al.* 2000; Armenio & Sarkar 2002; Iida *et al.* 2002; Garcia-Villalba & Del Alamo 2011), in the Appendix we conduct additional simulations by doubling the domain length and width. The results seem to suggest that the domain sizes indeed have some influence on the flow transitional behaviour (possibly also relaminarization). To fully put this question to rest, clearly far more detailed studies have to be carried out in much larger domain sizes. Instead of remaining constant as in incompressible flows, C_f for the relaminarized case

https://doi.org/10.1017/jfm.2019.727 Published online by Cambridge University Press

undergoes periodic oscillations for the supersonic case. By employing phase and Farve averaging, we demonstrate that the instantaneous Reynolds shear stress is non-zero even for the relaminarized case, which is due to periodic variation of density caused by wall actuation. In addition, the skin-friction decomposition using the FIK identity reveals that the compressible contribution C_f^{μ} continuously increases with A^+, which is due to increased viscosity caused by SWO. This indicates that $\mathcal{DR}$ might be decreased at very high A^+, where the compressibility contribution C_f^{μ} becomes significant – distinctly different from the incompressible case (Quadrio & Ricco 2004).

The Reynolds number effect on drag control is also studied with additional simulations at a higher $Re_b = 7667$ at $M_b = 0.8$ and $M_b = 1.5$. Similar to that observed for the strictly incompressible case (Hurst *et al.* 2014; Yao *et al.* 2019), $\mathcal{DR}$ is less affected with increasing Re_b at small T^+ but deteriorates rapidly at large T^+. Assuming $\mathcal{DR} \propto Re_\tau^{-\gamma}$, the scaling exponent γ for the $M_b = 0.8$ case increases from 0.1 for $T^+ = 25$ to 0.49 for $T^+ = 300$. In addition, the optimal oscillation period at $M_b = 0.8$ shifts to smaller values $T^+_{opt} = 100$ with $\mathcal{DR}_{max} = 30.3\,\%$. For the $M_b = 1.5$ case, $\mathcal{DR}$ becomes non-monotonically varying with T^+ at $Re_b = 7667$, with $\mathcal{DR}_{max}$ of 33.7 % at $T^+ = 150$. To illustrate the reason for the deterioration of $\mathcal{DR}$ at high Re_b, flow statistics between two different Re_b cases are analysed for $M_b = 1.5$ at the near-optimal control period $T^+ = 150$. Using the Trettel–Larsson transformation, the upward shift of the streamwise mean velocity profiles under control decreases as Re_b increases, akin to incompressible flows (Hurst *et al.* 2014; Yao *et al.* 2019). The analysis also shows that, as Re_b increases, the control becomes less effective for suppressing turbulent fluctuation, especially in the near-wall region.

Finally, the drag control performance is compared between the supersonic $M_b = 1.5$ and the strictly incompressible cases at comparable $Re^*_{\tau c}$, where the mean velocity, Reynolds stresses and also the near-wall streaks for the uncontrolled cases are found to be well matched in semi-local units with the only exception being the peak of the streamwise turbulent stress. Compared with the incompressible cases, the optimal oscillation period T^+_{opt} for the supersonic case in wall units becomes large. Employing a simple scaling for the oscillation period $T^* = T_C^+ l_I^+ / l_C^+$, $\mathcal{DR}$ exhibits a better match between the supersonic and incompressible cases with $T^*_{opt} = 100$, except for slightly higher $\mathcal{DR}$ obtained for the supersonic cases. Note that the simple scaling based on (4.1) roughly predicts the optimal oscillation period for different M_b cases, which enables selection of the control parameters for the compressible flows using results from the incompressible studies. This scaling also guides an estimation of $\mathcal{DR}$ for the compressible flows. However, a comprehensive model which can incorporate more aspects, like the oscillating amplitude effect, might be plausible. Based on the interaction of spanwise Stokes layer and the near-wall turbulence, Choi *et al.* (2002) derived a linear relationship between $\mathcal{DR}$ and a parameter V_c^+, which is a function of the thickness and acceleration of the Stokes layer and depends on the oscillation parameters. It well characterizes $\mathcal{DR}$ for the small oscillation period (i.e. $T^+ < 150$). If a good approximation of the Stokes layer solution can be derived for compressible flows, it might be feasible to extend this model to incorporate the M_b effect. Although the incompressible laminar analytical solution loses its validity for compressible flows, it might still be possible to exploit it as a first-order approximation based on our observation that the phase-averaged spanwise velocity from DNS does not significantly deviate from it very close to the wall.

Current results show that, as M_b increases, the fluctuations of thermodynamic properties progressively affect drag reduction performance, because the fluctuations

https://doi.org/10.1017/jfm.2019.727 Published online by Cambridge University Press

Case	Re_τ	$Re^*_{\tau c}$	$L_x \times L_y \times L_z$	$N_x \times N_y \times N_z$	$C_f \times 10^3$	$\mathcal{DR}$ (%)
D0	219.3	144.7	$6\pi h \times 2h \times 2\pi h$	$512 \times 129 \times 256$	7.81 ± 0.05	36.4 ± 0.9
D1	219.6	144.8	$12\pi h \times 2h \times 4\pi h$	$1024 \times 129 \times 512$	7.88 ± 0.02	35.9 ± 0.5

TABLE 3. Parameters used in the study of domain size effect for supersonic case at $Re_b = 3000$ and $M_b = 1.5$. Here, C_f values are for the uncontrolled case and $\mathcal{DR}$ values are the amount of drag reduction for SWO with $T^+ = 100$ and $A^+ = 12$.

would also contribute to the mean skin friction, especially for SWO with small T^+. Future work might include the study of drag control at even higher Mach number, where the thermodynamic fluctuations become significant. Similar to the incompressible cases, the turbulent contribution for the skin friction continuously increases with Re_b for the compressible cases also. Hence, it would be necessary to investigate the similarity between incompressible and compressible flows at high Reynolds numbers. In addition, since the main objective of skin-friction drag control is to suppress turbulence to achieve net power savings, it would be worthwhile to investigate the effects of Mach number, Reynolds number as well as the control parameters on energy cost and net energy saving rate.

Acknowledgements

Computational resources provided by Texas Tech University HPCC and TACC Lonestar are acknowledged. Post-processing resources were provided by XSEDE under allocation number CTS-180032. We are grateful to C. Bryson and E. Stout for review of the manuscript. We also appreciate Lee and Moser for providing us their incompressible DNS code, which is used for this study.

Appendix. Effect of computational domain size

The effect of computational domain size on DNS of incompressible turbulent channels flows has been extensively studied. For example, Lozano-Duran & Jiménez (2014) showed that a domain with streamwise and spanwise sizes of $2\pi h \times \pi h$ is large enough to produce reasonably good one-point statistics similar to those for larger domains. They argued that, because of the periodic boundary condition, the very large structures, if they do not fit within the smaller domain, behave like infinitely long structures, and that their interaction with small-scale structures is correctly captured. Gatti & Quadrio (2013) also studied the domain size effect on drag reduction using SWO. They found that, although the skin friction C_f tends to be underestimated as the domain size decreases, most of the inaccuracy in C_f cancels out when the two C_f terms (with and without control) are subtracted to compute drag reduction.

Although the domain size we employed here is relatively large, it might still be necessary to justify its adequacy, in particular for the supersonic cases, as the length scale of the structures continuously increases with M_b (see figure 14). Hence, an additional simulation of larger computational domain size is performed for the supersonic $Re_b = 3000$ and $M_b = 1.5$ case with the same grid resolution; see table 1. The computational domain size is doubled in both the streamwise ($L_x = 12\pi$) and spanwise ($L_z = 4\pi$) directions. The skin friction C_f values for the two different domain sizes are shown in table 3; the difference is found to be less than 1 %. This is consistent with the finding of Modesti & Pirozzoli (2016), who demonstrated that

https://doi.org/10.1017/jfm.2019.727 Published online by Cambridge University Press

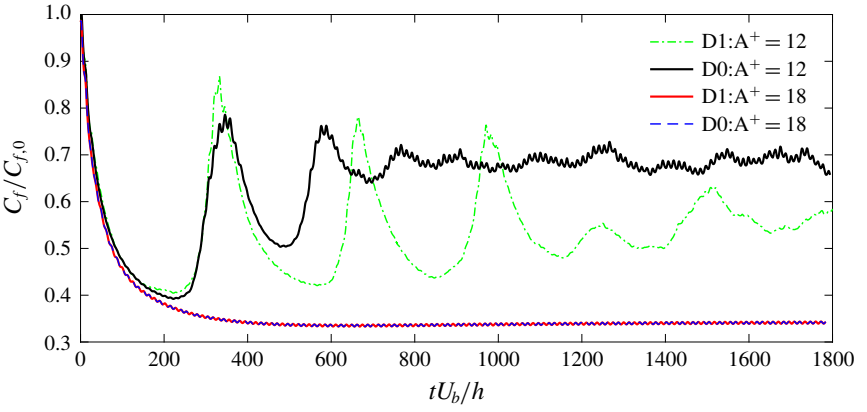


FIGURE 32. (Colour online) Time evolution of normalized skin friction $C_f/C_{f,0}$ for two different domain size cases at $T^+ = 300$ ($Re_b = 3000$ and $M_b = 1.5$).

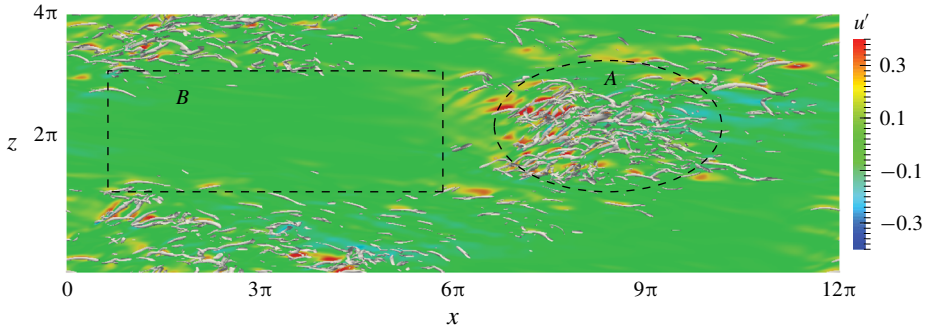


FIGURE 33. (Colour online) Top view of instantaneous streamwise velocity fluctuations u'/U_b in the x–z plane at $y^* = 15$ associated with λ_ρ vortical structures at $t = 1500h/U_b$ for the large-domain D1 case with $A^+ = 12$ and $T^+ = 300$.

the effect of enlarging the computational box size on turbulent statistics is marginal. As compared to C_f, the correct prediction of $\mathcal{DR}$ is more important for drag control studies. In addition to the uncontrolled case, wall oscillation simulations for $T^+ = 100$ and $A^+ = 12$ are also performed to ascertain the effect of domain size on $\mathcal{DR}$. The effect on $\mathcal{DR}$ is found to be smaller than 0.5 %.

To address the domain size effect on flow transition and relaminarization, two additional simulations for $A^+ = 12$ and 18 with $T^+ = 300$ are conducted using the larger domain size. Figure 32 compares the time evolution of normalized skin friction $C_f/C_{f,0}$ for two different domain size cases. For $A^+ = 18$, the flow also becomes relaminarized for the large-domain-size D1 case with C_f time evolution identical to that of the small-domain-size D0 case. However, for $A^+ = 12$, although C_f still experiences large oscillations, both the oscillation period and amplitude become smaller. Compared with the small-domain D0 case, C_f reaches the steady state earlier. Figure 33 further shows the near-wall streamwise velocity fluctuations associated with λ_ρ vortices for the larger-domain D1 case with $A^+ = 12$ at time $t = 1500h/U_b$. It is clear that, although C_f already reaches the steady state, there exist turbulent–laminar patches in the flow, which closely resemble other transitional wall-bounded flows

https://doi.org/10.1017/jfm.2019.727 Published online by Cambridge University Press

(Barkley & Tuckerman 2005; Duguet, Schlatter & Henningson 2010). The turbulent regions (e.g. A in figure 33) present the usual low- and high-speed streaks with titled vortices sitting on top of them (Yakeno *et al.* 2014; Yao *et al.* 2019). On the other hand, there are large laminar regions (B in figure 33), which are comparable to the computational box sizes used in the main study. This indicates that the limited domain size might be one possible reason for flow transition and relaminarization observed in § 3.8 and also here – similar to that observed for stably stratified turbulent flows. For example, Garg *et al.* (2000) reported transition and relaminarizaiton of the flow at relatively weak stratification, but later Garcia-Villalba & Del Alamo (2011) found that the transition and relaminarization were due to small-domain-size effect, and the flow can still reach a statistically steady state with a very large domain size.

REFERENCES

AGOSTINI, L., TOUBER, E. & LESCHZINER, M. A. 2014 Spanwise oscillatory wall motion in channel flow: drag-reduction mechanisms inferred from DNS-predicted phase-wise property variations at $Re_\tau = 1000$. *J. Fluid Mech.* **743**, 606–635.

ARMENIO, V. & SARKAR, S. 2002 An investigation of stably stratified turbulent channel flow using large-eddy simulation. *J. Fluid Mech.* **459**, 1–42.

BARKLEY, D. & TUCKERMAN, L. S. 2005 Computational study of turbulent laminar patterns in Couette flow. *Phys. Rev. Lett.* **94** (1), 014502.

BARON, A. & QUADRIO, M. 1995 Turbulent drag reduction by spanwise wall oscillations. *Appl. Sci. Res.* **55** (4), 311–326.

BATCHELOR, G. K. 1967 *An Introduction to Fluid Dynamics*. Cambridge University Press.

BECHERT, D. W., BRUSE, M., HAGE, W., VAN DER HOEVEN, J. G. T. & HOPPE, G. 1997 Experiments on drag-reducing surfaces and their optimization with an adjustable geometry. *J. Fluid Mech.* **338**, 59–87.

BERGER, T. W., KIM, J., LEE, C. & LIM, J. 2000 Turbulent boundary layer control utilizing the lorentz force. *Phys. Fluids* **12** (3), 631–649.

BERNARDINI, M., PIROZZOLI, S. & ORLANDI, P. 2014 Velocity statistics in turbulent channel flow up to $Re_\tau = 4000$. *J. Fluid Mech.* **742**, 171–191.

CHEN, J., HUSSAIN, F., PEI, J. & SHE, Z.-S. 2014 Velocity–vorticity correlation structure in turbulent channel flow. *J. Fluid Mech.* **742**, 291–307.

CHOI, H., MOIN, P. & KIM, J. 1994 Active turbulence control for drag reduction in wall-bounded flows. *J. Fluid Mech.* **262**, 75–110.

CHOI, J.-I., XU, C.-X. & SUNG, H. J. 2002 Drag reduction by spanwise wall oscillation in wall-bounded turbulent flows. *AIAA J.* **40** (5), 842–850.

COLEMAN, G. N., KIM, J. & MOSER, R. D. 1995 A numerical study of turbulent supersonic isothermal-wall channel flow. *J. Fluid Mech.* **305**, 159–183.

DENG, B.-Q., XU, C.-X., HUANG, W.-X. & CUI, G.-X. 2014 Strengthened opposition control for skin-friction reduction in wall-bounded turbulent flows. *J. Turbul.* **15** (2), 122–143.

VAN DRIEST, E. R. 1951 Turbulent boundary layer in compressible fluids. *J. Aeronaut. Sci.* **18** (3), 145–160.

DUAN, L., BEEKMAN, I. & MARTIN, M. P. 2010 Direct numerical simulation of hypersonic turbulent boundary layers. Part 2. Effect of wall temperature. *J. Fluid Mech.* **655**, 419–445.

DUAN, L. & CHOUDHARI, M. 2012 Effects of riblets on skin friction and heat transfer in high-speed turbulent boundary layers. In *50th AIAA Aerospace Sciences Meeting including the New Horizons Forum and Aerospace Exposition*, *AIAA Paper* 2012-1108.

DUAN, L. & CHOUDHARI, M. M. 2014 Direct numerical simulations of high-speed turbulent boundary layers over riblets. In *52nd Aerospace Sciences Meeting*, *AIAA Paper* 2014-0934.

DUGUET, Y., SCHLATTER, P. & HENNINGSON, D. S. 2010 Formation of turbulent patterns near the onset of transition in plane Couette flow. *J. Fluid Mech.* **650**, 119–129.

https://doi.org/10.1017/jfm.2019.727 Published online by Cambridge University Press

FANG, J., LU, L.-P. & SHAO, L. 2010 Heat transport mechanisms of low Mach number turbulent channel flow with spanwise wall oscillation. *Acta Mech. Sin.* **26** (3), 391–399.

FOYSI, H., SARKAR, S. & FRIEDRICH, R. 2004 Compressibility effects and turbulence scalings in supersonic channel flow. *J. Fluid Mech.* **509**, 207–216.

FUKAGATA, K., IWAMOTO, K. & KASAGI, N. 2002 Contribution of Reynolds stress distribution to the skin friction in wall-bounded flows. *Phys. Fluids* **14** (11), L73–L76.

GARCÍA-MAYORAL, R. & JIMÉNEZ, J. 2011 Drag reduction by riblets. *Phil. Trans. R. Soc. Lond.* A **369** (1940), 1412–1427.

GARCIA-VILLALBA, M. & DEL ALAMO, J. C. 2011 Turbulence modification by stable stratification in channel flow. *Phys. Fluids* **23** (4), 045104.

GARG, R. P., FERZIGER, J. H., MONISMITH, S. G. & KOSEFF, J. R. 2000 Stably stratified turbulent channel flows. I. Stratification regimes and turbulence suppression mechanism. *Phys. Fluids* **12** (10), 2569–2594.

GATTI, D. & QUADRIO, M. 2013 Performance losses of drag-reducing spanwise forcing at moderate values of the Reynolds number. *Phys. Fluids* **25** (12), 125109.

GATTI, D. & QUADRIO, M. 2016 Reynolds-number dependence of turbulent skin-friction drag reduction induced by spanwise forcing. *J. Fluid Mech.* **802**, 553–582.

GOMEZ, T., FLUTET, V. & SAGAUT, P. 2009 Contribution of Reynolds stress distribution to the skin friction in compressible turbulent channel flows. *Phys. Rev.* E **79** (3), 035301.

GUALA, M., HOMMEMA, S. E. & ADRIAN, R. J. 2006 Large-scale and very-large-scale motions in turbulent pipe flow. *J. Fluid Mech.* **554**, 521–542.

HACK, M. J. P. & ZAKI, T. A. 2014 The influence of harmonic wall motion on transitional boundary layers. *J. Fluid Mech.* **760**, 63–94.

HADJADJ, A., BEN-NASR, O., SHADLOO, M. S. & CHAUDHURI, A. 2015 Effect of wall temperature in supersonic turbulent boundary layers: a numerical study. *Intl J. Heat Mass Transfer* **81**, 426–438.

HUANG, P. G., COLEMAN, G. N. & BRADSHAW, P. 1995 Compressible turbulent channel flows: DNS results and modelling. *J. Fluid Mech.* **305**, 185–218.

HURST, E., YANG, Q. & CHUNG, Y. M. 2014 The effect of Reynolds number on turbulent drag reduction by streamwise travelling waves. *J. Fluid Mech.* **759**, 28–55.

HUTCHINS, N. & MARUSIC, I. 2007 Evidence of very long meandering features in the logarithmic region of turbulent boundary layers. *J. Fluid Mech.* **579**, 1–28.

IIDA, O., KASAGI, N. & NAGANO, Y. 2002 Direct numerical simulation of turbulent channel flow under stable density stratification. *Intl J. Heat Mass Transfer* **45** (8), 1693–1703.

JIMÉNEZ, J. 2004 Turbulent flows over rough walls. *Annu. Rev. Fluid Mech.* **36**, 173–196.

JUNG, W. J., MANGIAVACCHI, N. & AKHAVAN, R. 1992 Suppression of turbulence in wall-bounded flows by high-frequency spanwise oscillations. *Phys. Fluids* A **4** (8), 1605–1607.

KAMETANI, Y. & FUKAGATA, K. 2011 Direct numerical simulation of spatially developing turbulent boundary layers with uniform blowing or suction. *J. Fluid Mech.* **681**, 154–172.

KAMETANI, Y., FUKAGATA, K., ÖRLÜ, R. & SCHLATTER, P. 2015 Effect of uniform blowing/suction in a turbulent boundary layer at moderate Reynolds number. *Intl J. Heat Fluid Flow* **55**, 132–142.

KAMETANI, Y., KOTAKE, A., FUKAGATA, K. & TOKUGAWA, N. 2017 Drag reduction capability of uniform blowing in supersonic wall-bounded turbulent flows. *Phys. Rev. Fluids* **2** (12), 123904.

KIM, J., MOIN, P. & MOSER, R. 1987 Turbulence statistics in fully developed channel flow at low Reynolds number. *J. Fluid Mech.* **177**, 133–166.

LAADHARI, F., SKANDAJI, L. & MOREL, R. 1994 Turbulence reduction in a boundary layer by a local spanwise oscillating surface. *Phys. Fluids* **6** (10), 3218–3220.

LARDEAU, S. & LESCHZINER, M. A. 2013 The streamwise drag-reduction response of a boundary layer subjected to a sudden imposition of transverse oscillatory wall motion. *Phys. Fluids* **25** (7), 075109.

LEE, M. & MOSER, R. D. 2015 Direct numerical simulation of turbulent channel flow up to $Re = 5200$. *J. Fluid Mech.* **774**, 395–415.

https://doi.org/10.1017/jfm.2019.727 Published online by Cambridge University Press

LOZANO-DURÁN, A. & JIMÉNEZ, J. 2014 Effect of the computational domain on direct simulations of turbulent channels up to $Re_\tau = 4200$. *Phys. Fluids* **26** (1), 011702.

LOZANO-DURAN, A. & JIMÉNEZ, J. 2014 Effect of the computational domain on direct simulations of turbulent channels up to $Re_\tau = 4200$. *Phys. Fluids* **26** (1), 011702.

MARUSIC, I., MATHIS, R. & HUTCHINS, N. 2010 Predictive model for wall-bounded turbulent flow. *Science* **329** (5988), 193–196.

MIN, T. & KIM, J. 2004 Effects of hydrophobic surface on skin-friction drag. *Phys. Fluids* **16** (7), L55–L58.

MITTAL, R. & MOIN, P. 1997 Suitability of upwind-biased finite difference schemes for large-eddy simulation of turbulent flows. *AIAA J.* **35** (8), 1415–1417.

MOARREF, R. & JOVANOVIĆ, M. R. 2012 Model-based design of transverse wall oscillations for turbulent drag reduction. *J. Fluid Mech.* **707**, 205–240.

MODESTI, D. & PIROZZOLI, S. 2016 Reynolds and Mach number effects in compressible turbulent channel flow. *Intl J. Heat Fluid Flow* **59**, 33–49.

MORINISHI, Y., TAMANO, S. & NAKABAYASHI, K. 2004 Direct numerical simulation of compressible turbulent channel flow between adiabatic and isothermal walls. *J. Fluid Mech.* **502**, 273–308.

NAKANISHI, R., MAMORI, H. & FUKAGATA, K. 2012 Relaminarization of turbulent channel flow using traveling wave-like wall deformation. *Intl J. Heat Fluid Flow* **35**, 152–159.

NI, W., LU, L., RIBAULT, C. L. & FANG, J. 2016 Direct numerical simulation of supersonic turbulent boundary layer with spanwise wall oscillation. *Energies* **9** (3), 154.

OLIVER, T. A., MALAYA, N., ULERICH, R. & MOSER, R. D. 2014 Estimating uncertainties in statistics computed from direct numerical simulation. *Phys. Fluids* **26** (3), 035101.

ORLANDI, P. & FATICA, M. 1997 Direct simulations of turbulent flow in a pipe rotating about its axis. *J. Fluid Mech.* **343**, 43–72.

PATEL, A., BOERSMA, B. J. & PECNIK, R. 2016 The influence of near-wall density and viscosity gradients on turbulence in channel flows. *J. Fluid Mech.* **809**, 793–820.

PATEL, A., PEETERS, J. W. R., BOERSMA, B. J. & PECNIK, R. 2015 Semi-local scaling and turbulence modulation in variable property turbulent channel flows. *Phys. Fluids* **27** (9), 095101.

PIROZZOLI, S. & BERNARDINI, M. 2011 Turbulence in supersonic boundary layers at moderate Reynolds number. *J. Fluid Mech.* **688**, 120–168.

QUADRIO, M. & RICCO, P. 2003 Initial response of a turbulent channel flow to spanwise oscillation of the walls. *J. Turbul.* **4** (7), 1–23.

QUADRIO, M. & RICCO, P. 2004 Critical assessment of turbulent drag reduction through spanwise wall oscillations. *J. Fluid Mech.* **521**, 251–271.

QUADRIO, M., RICCO, P. & VIOTTI, C. 2009 Streamwise-travelling waves of spanwise wall velocity for turbulent drag reduction. *J. Fluid Mech.* **627**, 161–178.

QUADRIO, M. & SIBILLA, S. 2000 Numerical simulation of turbulent flow in a pipe oscillating around its axis. *J. Fluid Mech.* **424**, 217–241.

RAI, M. M. & MOIN, P. 1991 Direct simulations of turbulent flow using finite-difference schemes. *J. Comput. Phys.* **96** (1), 15–53.

RICCO, P. & QUADRIO, M. 2008 Wall-oscillation conditions for drag reduction in turbulent channel flow. *Intl J. Heat Fluid Flow* **29** (4), 891–902.

ROTHSTEIN, J. P. 2010 Slip on superhydrophobic surfaces. *Annu. Rev. Fluid Mech.* **42**, 89–109.

SCHOPPA, W. & HUSSAIN, F. 1998 A large-scale control strategy for drag reduction in turbulent boundary layers. *Phys. Fluids* **10** (5), 1049–1051.

SCHOPPA, W. & HUSSAIN, F. 2002 Coherent structure generation in near-wall turbulence. *J. Fluid Mech.* **453**, 57–108.

SCIACOVELLI, L., CINNELLA, P. & GLOERFELT, X. 2017 Direct numerical simulations of supersonic turbulent channel flows of dense gases. *J. Fluid Mech.* **821**, 153–199.

SKOTE, M., MISHRA, M. & WU, Y. 2015 Drag reduction of a turbulent boundary layer over an oscillating wall and its variation with Reynolds number. *Intl J. Aerosp. Engng* **2015**, 891037.

SKOTE, M., MISHRA, M. & WU, Y. 2019 Wall oscillation induced drag reduction zone in a turbulent boundary layer. *Flow Turbul. Combust.* **102**, 641–666.

https://doi.org/10.1017/jfm.2019.727 Published online by Cambridge University Press

SPALART, P. R. & MCLEAN, J. D. 2011 Drag reduction: enticing turbulence, and then an industry. *Phil. Trans. R. Soc. Lond.* A **369** (1940), 1556–1569.

TOUBER, E. & LESCHZINER, M. A. 2012 Near-wall streak modification by spanwise oscillatory wall motion and drag-reduction mechanisms. *J. Fluid Mech.* **693**, 150–200.

TRETTEL, A. & LARSSON, J. 2016 Mean velocity scaling for compressible wall turbulence with heat transfer. *Phys. Fluids* **28** (2), 026102.

WANG, Y.-S., HUANG, W.-X. & XU, C.-X. 2016 Active control for drag reduction in turbulent channel flow: the opposition control schemes revisited. *Fluid Dyn. Res.* **48** (5), 055501.

XU, C.-X. & HUANG, W.-X. 2005 Transient response of Reynolds stress transport to spanwise wall oscillation in a turbulent channel flow. *Phys. Fluids* **17** (1), 018101.

YAKENO, A., HASEGAWA, Y. & KASAGI, N. 2014 Modification of quasi-streamwise vortical structure in a drag-reduced turbulent channel flow with spanwise wall oscillation. *Phys. Fluids* **26** (8), 085109.

YAO, J., CHEN, X. & HUSSAIN, F. 2018 Drag control in wall-bounded turbulent flows via spanwise opposed wall-jet forcing. *J. Fluid Mech.* **852**, 678–709.

YAO, J., CHEN, X. & HUSSAIN, F. 2019 Reynolds number effect on drag control via spanwise wall oscillation in turbulent channel flows. *Phys. Fluids* **31** (8), 085108.

YAO, J., CHEN, X., THOMAS, F. & HUSSAIN, F. 2017 Large-scale control strategy for drag reduction in turbulent channel flows. *Phys. Rev. Fluids* **2**, 062601.

YAO, J. & HUSSAIN, F. 2018 Toward vortex identification based on local pressure-minimum criterion in compressible and variable density flows. *J. Fluid Mech.* **850**, 5–17.

ZHANG, C., DUAN, L. & CHOUDHARI, M. M. 2018 Direct numerical simulation database for supersonic and hypersonic turbulent boundary layers. *AIAA J.* **56** (11), 4297–4311.

ZHE, C., CHANGPING, Y., LI, L. & XINLIANG, L. 2016 Effect of uniform blowing or suction on hypersonic spatially developing turbulent boundary layers. *Sci. Chin. Phys. Mech. Astron.* **59** (6), 664702.

https://doi.org/10.1017/jfm.2019.727 Published online by Cambridge University Press